PHILOSOPHICAL TRANSACTIONS OF THE ROYAL SOCIETY A
MATHEMATICAL, PHYSICAL & ENGINEERING SCIENCES

Numerical and Asymptotic Methods for Certain Viscous Free-Surface Flows

W. G. Pritchard, L. R. Scott and S. J. Tavener

Phil. Trans. R. Soc. Lond. A 1992 **340**, 1-45
doi: 10.1098/rsta.1992.0054

Numerical and asymptotic methods for certain viscous free-surface flows

By W. G. Pritchard[1], L. R. Scott[2] and S. J. Tavener[1]

[1] *Department of Mathematics, Pennsylvania State University, University Park, Pennsylvania 16802, U.S.A.*

[2] *Department of Mathematics, University of Houston, Houston, Texas 77204, U.S.A.*

Contents

This paper concerns the two-dimensional motion of a viscous liquid down a perturbed inclined plane under the influence of gravity, and the main goal is the prediction of the surface height as the fluid flows over the perturbations. The specific perturbations chosen for the present study were two humps stretching laterally across an otherwise uniform plane, with the flow being confined in the lateral direction by the walls of a channel. Theoretical predictions of the flow have been obtained by finite-element approximations to the Navier–Stokes equations and also by a variety of lubrication approximations. The predictions from the various models are compared with experimental measurements of the free-surface profiles. The principal aim of this study is the establishment and assessment of certain numerical and asymptotic models for the description of a class of free-surface flows, exemplified by the particular case of flow over a perturbed inclined plane.

The laboratory experiments were made over a range of flow rates such that the

Phil. Trans. R. Soc. Lond. A (1992) **340**, 1–45

Printed in Great Britain

1

Vol. 340. A (15 July 1992)

Reynolds number, based on the volume flux per unit width and the kinematical viscosity of the fluid, ranged between 0.369 and 36.6. It was found that, at the smaller Reynolds numbers, a standard lubrication approximation provided a very good representation of the experimental measurements but, as the flow rate was increased, the standard model did not capture several important features of the flow. On the other hand, a lubrication approximation allowing for surface tension and inertial effects expanded the range of applicability of the basic theory by almost an order of magnitude, up to Reynolds numbers approaching 10. At larger flow rates, numerical solutions to the full equations of motion provided a description of the experimental results to within about 4%, up to a Reynolds number of 25, beyond which we were unable to obtain numerical solutions. It is not known why numerical solutions were not possible at larger flow rates, but it is possible that there is a bifurcation of the Navier–Stokes equations to a branch of unsteady motions near a Reynolds number of 25.

1. Introduction

This paper describes the results of a combined theoretical, experimental and computational study of the free-surface flow that arises when a sheet of fluid runs down a perturbed inclined plane under the action of gravity. One of the main reasons for interest in this kind of flow is to establish the efficacy of various asymptotic and numerical methods in describing viscous free-surface flows that arise in a practical context. The particular flow that has been chosen is one of the simplest we have been able to devise for which the related mathematical problem realizes a good theoretical representation and yet the flow provides a significant test of the solution procedures. That this goal has been achieved will become apparent as the discussion unfolds, but suffice it to say that, during the course of the research programme, we have found that one of the numerical schemes we had intended to use was, surprisingly, not a viable possibility without considerable modification (see Brenner *et al*. 1992) and, in another situation, the experimental results have proved extremely helpful in the development and testing of a new free-surface solver (Cliffe *et al*. 1992). Other methods we have used required the use of unexpectedly fine meshes to achieve the desired accuracy, and considerable care was needed to obtain convergence of the (iterative) numerical procedures. These experiences suggest the need for care when solving flows in more complicated domains and when attempting to model flows with less stringent control over the conditions than could be realized in the present experiments.

The flow considered herein exemplifies a class of flows which arise frequently in applications associated with processing and manufacturing involving the use of thin films, a class of flows often referred to in the chemical engineering literature as 'coating flows'. A practical example of such a flow arises in the deposition of films onto celluloid; another practical application occurs in continuous-casting processes, and further examples are described in the forthcoming article by Pritchard *et al*. (1992). One of the main practical implications of the present study is the provision of a good estimate of ranges of parameters for which certain approximations, such as the lubrication approximation, yield a good representation of the experimental situation. In our view, definitive results of this kind are of great value in developing experience in the use of simplified models for the understanding of fluid motions.

There have been several studies of closely related flow problems in recent years. Hansen (1986) used boundary-integral methods to make numerical studies of the two-dimensional Stokes flow over an obstacle placed on a tilted plane, and (in 1987) he applied the same techniques to determine the shape of the free surface when fluid flows down a tilted plane into a large pool of the same liquid. Pozrikidis (1988) used a boundary-integral method for the Stokes equations to study the flow of a liquid film along a periodically structured wall. Several studies have been made of the so-called coating and rimming flows on the exterior and interior of a rotating cylinder. One of the pioneering studies was made by Moffatt (1977), and among the more recent are the studies by Preziosi & Joseph (1987, 1988) and Johnson (1988), from which papers other relevant references are readily available. Preziosi & Joseph considered the stability of this class of fluid motion and also made some interesting experimental studies of the two kinds of flow. They developed a lubrication approximation for such flows and found that the approximate models used to describe the flows gave quite good predictions of their experiments.

There are relatively few examples of practical fluid motions for which an absolute comparison between solutions of the Navier–Stokes equations and empirical data can readily be made. Several factors contribute to this situation. Most mathematical theories for the Navier–Stokes equations are based on flows in bounded domains, and it is most common that non-trivial flows are generated through the imposition of non-zero Dirichlet data for the velocity field over some portion of the boundary of the domain. The practicalities involved with the empirical measurement of such data can be tedious. In addition, great care must be exercised to ensure that inlet and exit velocity fields are closely maintained throughout the course of an experiment, and that they are reproducible from day to day. In general, complete characterizations of such velocity fields would need to be ascertained for every operating condition of the experiment.

One simple way of obviating this difficulty is to work with flows on unbounded domains for which the asymptotic structure of the flow field at infinity is known. Having to find a solution of the Navier–Stokes equation on an unbounded rather than a bounded domain may seem, at first sight, to be an undue complication. However, it has been shown by Amick (1977, 1978) and by Amick & Fraenkel (1980) that, by restricting attention to flows in certain classes of channels and pipes, it is possible to demonstrate the existence of a solution to the Navier–Stokes equation over a substantial range of Reynolds numbers. In the event that these channels or pipes approach a uniform width far upstream and downstream, Amick (1978) showed that the velocity fields in the pipes approach the appropriate Poiseuille distribution and that the rate of approach is exponential, at least when the Reynolds number is not too large. In a study done concurrently with the present work, Abergel & Bona (1992) have been able to obtain similar kinds of results, for the Stokes equations, for a free-surface flow down an inclined perturbed plane. The exponentially fast approach upstream and downstream of these flows to their asymptotic states means that, by introducing and removing the fluid through sufficiently long uniform regions, it is possible to obtain a very close approximation to the flow in the unbounded domain by the flow in a bounded domain. The empirical characterization of these flow states is often relatively straightforward and the experiment is usually quite robust in that small changes in the operating conditions lead only to small variations in the boundary data. These principles are at the heart of the design of the present experiment, and we shall see that a complete specification of the flow conditions can be made simply by measuring the depths of the incoming and outgoing streams, once the basic material properties are known.

The structure of the paper is as follows. In §2 we give the theoretical background to the study. The mathematical problem used to model the experiments is presented and a variational formulation of the problem is described to set the scene for the numerical computations. An approximation to the complete mathematical problem can be obtained through the use of the lubrication approximation and a description of a model obtained through such an approach is given in §2*c*. Then, to round off the theoretical discussion, a brief description is given of the calculational procedures used in the numerical schemes.

The experimental methods are discussed and a complete description of the experimental apparatus is given in §3. Then, in §4*a*, a brief description is given of some test calculations made with the code before we embark on the detailed comparisons between the theoretical predictions and the experiments in §4*b*–*d*.

2. Theory

(*a*) *The mathematical model*

Consider flow in a channel of width w, the bed of which is located at a height $\tilde{b}(\tilde{x})$ above a plane that slopes at an angle α to the horizontal, where $\tilde{b}$ is measured in the direction $\tilde{y}$ normal to the plane. Let the origin for the coordinate frame $(\tilde{x}, \tilde{y})$ be located in this plane. We shall assume that $\tilde{b}(\tilde{x})$ is smooth and bounded and that $\tilde{b}$ is supported on a compact set of $\tilde{x}$. Denote $\max\{|\tilde{b}(\tilde{x})|\}$ by b_0.

Let the height of the free surface above the reference plane, in the direction $\tilde{y}$, be $\tilde{\zeta}(\tilde{x})$, and suppose that $\tilde{\zeta} \rightarrow H$ as $\tilde{x} \rightarrow \pm\infty$. (We shall suppose throughout that $\tilde{\zeta}$ is a single-valued function of $\tilde{x}$.) Let Q be the volume flow per unit width down the plane and let Ω denote the flow domain and write $\partial\Omega$ for the boundary of Ω. We shall use the length scale H to characterize Ω and let $U := (Q/H)$ be representative of the velocity field. For the time being it will be convenient to non-dimensionalize all variables with respect to these scales, and henceforth it will be assumed that variables are in dimensionless form unless otherwise stated. The liquid to be used for the experimental observations appears to conform closely to the Navier–Stokes model (see Pritchard 1986). Thus, if we let $\boldsymbol{u}(\boldsymbol{x})$ denote the fluid velocity at position $\boldsymbol{x} \in \Omega$ and let $p(\boldsymbol{x})$ denote the pressure, then the dynamical equations governing steady fluid motions in Ω are

$$R(\boldsymbol{u} \cdot \nabla)\,\boldsymbol{u} = -\nabla p + \Delta \boldsymbol{u} - G\boldsymbol{j}, \tag{2.1}$$

and

$$\operatorname{div}(\boldsymbol{u}) = 0. \tag{2.2}$$

Here $\boldsymbol{j}$ is the unit vector in the vertically upward direction, $R := UH/\nu\ (= Q/\nu)$ and $G := gH^2/\nu U$. In the above definitions ν is the kinematical viscosity of the fluid and g is the gravity constant. The quantity R, the Reynolds number, characterizes the relative importance of inertial and viscous stresses, and G is the gravity parameter, typifying the relative importance of the body forces due to gravity and the viscous stress field. Note that $(R/G)^{\frac{1}{2}} = U/(gH)^{\frac{1}{2}}$ is the parameter usually referred to as the Froude number, F. (The gravity parameter G took the value 40.9 in the experiments, F ranged between 0.09 and 0.95, and the Reynolds number between 0.37 and 37.)

The stress tensor $\sigma(\boldsymbol{x})$, which is scaled by $(\rho\nu U/H)$, where ρ is the fluid density, is given in rectangular coordinates, by

$$\sigma_{ij} := -p\delta_{ij} + (u_{i,j} + u_{j,i}). \tag{2.3}$$

The boundary conditions applying to (2.1) take two forms. On part of the boundary Γ_D, say, pure Dirichlet-type conditions apply, and on the remainder of the boundary, Γ_F (the free surface), a combination of Dirichlet and stress conditions obtain. These conditions are as follows.

(i) The Dirichlet conditions are that

$$\boldsymbol{u}(\boldsymbol{x}) = \boldsymbol{g}(\boldsymbol{x}) \quad \text{for} \quad \boldsymbol{x} \in \Gamma_D, \tag{2.4}$$

where $\boldsymbol{g}$ is some prescribed velocity field (compatible with (2.2)).

(ii) On the set Γ_F, representing the free surface, there is a kinematical constraint to be satisfied which, for steady flows, is that the velocity field at the free surface be tangential to the surface itself. Let $\boldsymbol{n}(\boldsymbol{x})$ and $\boldsymbol{t}(\boldsymbol{x})$ be mutually orthogonal unit vectors at each point $\boldsymbol{x} \in \Gamma_F$, with $\boldsymbol{n}$ normal to the surface and directed out of Ω. Then the kinematical constraint is simply

$$\boldsymbol{u}(\boldsymbol{x}) \cdot \boldsymbol{n} = 0 \quad \text{for} \quad \boldsymbol{x} \in \Gamma_F. \tag{2.5}$$

The boundary conditions on Γ_F arising from dynamical considerations relate to the stress field:

(*a*) a shear-stress condition, namely

$$\sigma_{ij} n_i t_j = 0; \tag{2.6}$$

(*b*) the normal-stress condition,

$$\sigma_{ij} n_i n_j = (T/\rho\nu U)\,\kappa, \tag{2.7}$$

where κ is the curvature of the surface, reckoned positive when the radius of curvature is directed into Ω, and T is the surface tension. Define $S := (T/\rho\nu U)$, which we shall refer to as the surface-tension parameter. In the experiments, S ranged between 34 and 1.7.

Consider, for the present, the problem posed by (2.1)–(2.7) on a finite domain terminated upstream at $x = x_A$ and downstream at $x = x_B$, say. A possible procedure for determining the unknown location of Γ_F is to use the following iterative method. Suppose that Γ_F^0 is some given approximation to the free surface. Then, for sufficiently small values of R, the boundary-value problem posed by (2.1) and (2.2), together with conditions (2.4)–(2.6) applying on the domain bounded by Γ_F^0, has a unique solution (see Solonnikov & Shchadilov 1973). Thus, a natural way to study the complete free-boundary problem, including the condition (2.7), is to solve (2.1) and (2.2), subject to conditions (2.4)–(2.6), with different choices of Γ_F^i, $i = 0, 1, 2, \ldots$, for the location of the free surface, until the condition (2.7) is satisfied. Since the curvature, κ, represents an elliptic differential operator, the condition (2.7) can be used in an iterative procedure to define a new approximation to Γ_F^i, where the left-hand side is evaluated by using the velocity and pressure fields computed on the previous domain. Boundary conditions on Γ_F^i, implicit in the formulation of the complete problem, are needed to fix the solution to (2.7) at each stage of the iteration. Possibilities that make (2.7) well posed (and see Pritchard *et al.* (1992) for a more detailed discussion) are Dirichlet conditions, $\zeta(x) = H$ at $x = x_A$, x_B, or Neumann conditions, $\zeta'(x_A) = \gamma_A$ and $\zeta'(x_B) = \gamma_B$, say, where γ_A, γ_B are specified slopes. Appropriate combinations of these conditions could also be used. (In the case that pure Neumann data are specified, a further condition would be needed to specify the integral of $(\zeta - H)$.) This approach to solving the free-boundary problem has been taken independently by Jean (1980) and by Solonnikov (1980). They showed for domains of finite extent, in which the free-surface terminates at a solid wall, at a specified angle, the iterative process just described forms a contraction in suitable Hölder spaces, when R is sufficiently small.

In some research done concurrently with the present study, Abergel & Bona (1992) have developed a mathematical theory for steady flows in a channel of infinite length. They have been able to show, for Stokes flows (i.e. for $R = 0$) and for sufficiently small values of b_0, that the complete free-boundary problem (2.1)–(2.7) has a steady solution and that the surface depth $\zeta(x)$ tends exponentially to the limiting depth H as $x \rightarrow \pm\infty$. The method of proof used by Abergel & Bona is to utilize the implicit function theorem to demonstrate the existence of a branch of solutions emanating from the flow down a plane channel as the perturbations are smoothly introduced. This theory, together with the exponential decay to the asymptotic states suggests that the problem can be efficiently approximated by truncating the x variable and solving an analogous problem on the finite domain $x_{\mathrm{A}} < x < x_{\mathrm{B}}$. The boundary condition on the depth, ζ, then becomes some combination of $\zeta(x_{\mathrm{A}}), \zeta(x_{\mathrm{B}}) = H$ and $\zeta'(x_{\mathrm{A}}), \zeta'(x_{\mathrm{B}}) = 0$ (one of each condition at each point, x_{A} and x_{B}). If the Neumann condition is specified at both ends, then the volume of $\boldsymbol{\Omega}$ (that is, the integral of ζ) must be specified. It should, however, be noted that there is as yet no existence theory for the present flow problem on the truncated domain (see Pritchard *et al.* (1992) for further details).

The difference between the problem encountered here and that considered by Jean (1980) and Solonnikov (1980) is that, in the present case, the Dirichlet data are non-zero at the points where Γ_{F} meets Γ_{D}, so that compatibility conditions between the surface slopes and the Dirichlet data must be met at these points. Moreover, this compatibility constraint will, in general, change with each iteration Γ_{F}^{i} of the free surface. Thus, if the slope of the free-surface is specified say at x_{A}, then the depth $\zeta(x_{\mathrm{A}})$ is unknown and the domain of definition of $\boldsymbol{g}$ (cf. (2.4)) must be scaled appropriately to accommodate the changing depth with each iteration. If, on the other hand, the depth at x_{A} is specified, then the slope of Γ_{F} is unknown there, and $\boldsymbol{g}$ must be chosen appropriately to ensure compatibility with the free-surface condition on Γ_{F}, namely that the component of $\boldsymbol{u}$ normal to Γ_{F} be zero. For the present flow it seems natural to represent the inlet and exit flows by specifying *a priori* the normal component of $\boldsymbol{g}$ on Γ_{D} and choosing the tangential component in such a way that the compatibility with Γ_{F} is satisfied at each stage of the iteration.

The stability of plane Poiseuille–Nusselt flow over an inclined plane (with $b = 0$ everywhere) has been widely studied. Benjamin (1957) and Yih (1963) (and see Yih 1969) showed, on the basis of the linearized equations, that the steady free-surface flow is unstable when the Reynolds number exceeds $\frac{5}{6}\cot\alpha$. These analyses were subsequently amplified by Shih & Shen (1975), who showed that the time-dependent linear problem is well posed. For Reynolds numbers only slightly in excess of the critical value the growth rates for this instability can be quite small (cf. §3*f* below).

(*b*) *Variational* (*weak*) *formulations*

Several variational formulations exist that are formally equivalent to the equations ((2.1) and (2.2)) (see Gunzburger 1989; Brenner *et al.* 1992). One such formulation, appropriate for the stress boundary conditions (2.6) and (2.7), is

$$a(\boldsymbol{u}, \boldsymbol{v}) + d(\boldsymbol{v}, p) = Rc(\boldsymbol{u}, \boldsymbol{u}, \boldsymbol{v}) - G\int_{\Omega} \boldsymbol{j}\cdot\boldsymbol{v}\,\mathrm{d}\boldsymbol{x}, \tag{2.8a}$$

and
$$d(\boldsymbol{u}, q) = 0, \tag{2.8b}$$
where the forms $a(\cdot,\cdot,\cdot)$, $c(\cdot,\cdot,\cdot)$ and $d(\cdot,\cdot)$ are defined as

$$a(\boldsymbol{u}, \boldsymbol{v}) := 2\int_{\Omega} \sum_{i,j=1}^{2} e_{ij}(\boldsymbol{u})\, e_{ij}(\boldsymbol{v})\,\mathrm{d}\boldsymbol{x}, \tag{2.9}$$

$$c(\boldsymbol{u}, \boldsymbol{v}, \boldsymbol{w}) := -\int_{\Omega} \sum_{i,j=1}^{2} u_i\, v_{j,i}\, w_j\,\mathrm{d}\boldsymbol{x}, \tag{2.10}$$

$$d(\boldsymbol{v}, q) := -\int_{\Omega} \sum_{i=1}^{2} v_{i,i}\, q\,\mathrm{d}\boldsymbol{x}, \tag{2.11}$$

and e_{ij} denotes the rate-of-strain tensor.

To be more precise about the variational formulation, we must define some standard spaces (definitions of which are given, for example, in Ciarlet's (1978) book). Let $L^r(\Omega)$ denote the Lebesgue space of rth power integrable functions on Ω, with norm denoted by $\|f\|_{L^r(\Omega)}$. In the special case $r=\infty$, $L^\infty(\Omega)$ denotes the space of functions bounded a.e. on Ω and $\|f\|_{L^\infty(\Omega)}$ is the essential supremum of $|f|$ on Ω. We let $W_r^k(\Omega)$ denote the Sobolev space of functions whose derivatives of order k, or less, are in $L^r(\Omega)$, with norm denoted by $\|f\|_{W_r^k(\Omega)}$. Note that $W_r^k(\Omega) = L^r(\Omega)$ when $k=0$, and the norms are equal as well. For vector-valued functions, we make analogous definitions. We say that $\boldsymbol{f} \in \boldsymbol{W}_r^k(\Omega)$ if each component f_1, f_2 of $\boldsymbol{f}$ is in $W_r^k(\Omega)$ and we define

$$\|\boldsymbol{f}\|_{\boldsymbol{W}_r^k(\Omega)} := (\|f_1\|^r_{W_r^k(\Omega)} + \|f_2\|^r_{W_r^k(\Omega)})^{1/r}, \quad 1 \leqslant r < \infty,$$
$$\|\boldsymbol{f}\|_{\boldsymbol{W}_\infty^k(\Omega)} := \max_{i=1,2} \|f_i\|_{W_\infty^k(\Omega)}.$$

For convenience we shall denote the Hilbert spaces $\boldsymbol{W}_2^k(\Omega)$ by $\boldsymbol{H}^k(\Omega)$.

Returning to the variational formulation, we define

$$\left.\begin{aligned} V &:= \{\boldsymbol{v} \in \boldsymbol{H}^1(\Omega) : \boldsymbol{v} = \boldsymbol{0} \text{ on } \Gamma_{\mathrm{D}}, \quad \text{and} \quad \boldsymbol{v}\cdot\boldsymbol{n} = 0 \text{ on } \Gamma_{\mathrm{F}}\}, \\ \Pi &:= \left\{q \in L^2(\Omega) : \int_{\Omega} q(\boldsymbol{x})\,\mathrm{d}\boldsymbol{x} = 0\right\}. \end{aligned}\right\} \tag{2.12}$$

Then (see, for example, Gunzburger 1989) the solution to (2.1) and (2.2), with (2.4)–(2.6), satisfies (2.8) for all $\boldsymbol{v} \in V$ and all $q \in \Pi$. Moreover, $\boldsymbol{u}$ and p can be characterized as solving the following variational problem.

Find $\boldsymbol{u}$ such that $\boldsymbol{u} - \boldsymbol{g} \in V$ and $p \in \Pi$ such that (2.8) holds for all $\boldsymbol{v} \in V$ and all $q \in \Pi$.

Here and below, it is assumed that the function $\boldsymbol{g}$ used to represent the Dirichlet boundary data (cf. (2.4)) has been extended appropriately to the domain Ω.

It is also possible to incorporate the free-surface equation (2.7) into a variational formulation (see, for example, Saito & Scriven 1981). The curvature κ can be written in terms of the fluid depth, ζ, as

$$\kappa(x, \zeta(x)) \left(= \frac{\theta'(x)}{s'(x)}\right) = -\frac{1}{s'(x)} \left(\frac{\zeta'(x)}{\surd(1+\zeta'(x)^2)}\right)', \tag{2.13}$$

where θ denotes the angle made between the tangent to the fluid surface and the x-axis, and s denotes arc length. Let $\boldsymbol{v} \in \boldsymbol{W}_r^1(\Omega)$ be such that $\boldsymbol{v} = \boldsymbol{0}$ on Γ_{D}, and define

$\chi := \boldsymbol{v}\cdot\boldsymbol{n}|_{\Gamma_F}$. Then, on multiplying (2.7) by $\chi s'(x)$, integrating over $[x_A, x_B]$ and making an integration by parts we find that

$$A(\zeta,\chi) := S\int_{x_A}^{x_B} \frac{\zeta'(x)\,\chi'(x)}{\surd(1+\zeta'(x)^2)}\,\mathrm{d}x = \int_{x_A}^{x_B} \sigma_{ij}\,n_i\,n_j\,\chi(s)\,s'(x)\,\mathrm{d}x,$$

$$= \int_{\Gamma_F} \sigma_{ij}\,n_i\,n_j\,\boldsymbol{v}\cdot\boldsymbol{n}\,\mathrm{d}s, \tag{2.14}$$

where the expression on the left-hand side is symbolized by $A(\zeta,\chi)$, as indicated. The latter term of (2.14), representing the normal load acting on the free surface Γ_F, can be converted to a volumetric term by taking a dot product by a function $\boldsymbol{v}$ throughout (2.1), integrating the resulting equation over the domain Ω and making an integration by parts. Then, by virtue of the boundary condition (2.6) and the continuity condition, it follows that

$$\oint_{\Gamma_F} \chi\sigma_{ij}\,n_i\,n_j\,\mathrm{d}s = a(\boldsymbol{u},\boldsymbol{v}) + d(\boldsymbol{v},p) - Rc(\boldsymbol{u},\boldsymbol{u},\boldsymbol{v}) + G\int_\Omega \boldsymbol{j}\cdot\boldsymbol{v}\,\mathrm{d}\boldsymbol{x},$$

which quantity we denote by the form $\phi(\boldsymbol{u},p,\boldsymbol{v})$, i.e.

$$\phi(\boldsymbol{u},p,\boldsymbol{v}) := a(\boldsymbol{u},\boldsymbol{v}) + d(\boldsymbol{v},p) - Rc(\boldsymbol{u},\boldsymbol{u},\boldsymbol{v}) + G\int_\Omega \boldsymbol{j}\cdot\boldsymbol{v}\,\mathrm{d}\boldsymbol{x}. \tag{2.15}$$

Then the free-surface height ζ can be characterized by the equation

$$A(\zeta,\chi) = \phi(\boldsymbol{u},p,\boldsymbol{v}), \tag{2.16}$$

with $\chi := \boldsymbol{v}\cdot\boldsymbol{n}|_{\Gamma_F}$. Note that, provided $r < 2$, it is possible to have $\chi(x_A)$, $\chi(x_B) \neq 0$, even though $\boldsymbol{v} = \boldsymbol{0}$ on Γ_D.

In the case that Dirichlet conditions are posed at the end points of the free-boundary, i.e. that $\zeta(x_A)$, $\zeta(x_B) = H$, then a natural space for χ in (2.16) is $\mathring{W}_1^1(x_A,x_B)$, where the overwritten zero indicates that we consider only the subset of admissible functions that vanish at x_A and x_B. In such a setting, (2.16) characterizes a unique solution ζ such that $\zeta - H \in \mathring{W}_\infty^1(x_A,x_B)$, which property ensures that Ω is a Lipschitz domain. The right-hand side of (2.16) depends only on the boundary values χ of $\boldsymbol{v}\cdot\boldsymbol{n}$, in view of (2.13): if $\boldsymbol{w}$ satisfies $\chi = \boldsymbol{w}\cdot\boldsymbol{n}|_{\Gamma_F}$, then $\boldsymbol{v} - \boldsymbol{w} \in V$ and

$$\phi(\boldsymbol{u},p,\boldsymbol{v}-\boldsymbol{w}) = 0.$$

The complete free-boundary problem (2.1)–(2.7) can now be characterized as being equivalent to the following variational problem.

Find functions $\boldsymbol{u}, p$ and ζ with the property that $\boldsymbol{u} - \boldsymbol{g} \in V$, $p \in \Pi$ and $\zeta - H \in \mathring{W}_\infty^1(x_A,x_B)$ such that

$$\left.\begin{aligned} \phi(\boldsymbol{u},p,\boldsymbol{v}) &= 0,\\ d(\boldsymbol{u},q) &= 0,\\ A(\zeta,\chi) &= \phi(\boldsymbol{u},p,\boldsymbol{E}\chi),\end{aligned}\right\} \tag{2.17}$$

for all $\boldsymbol{v} \in V$, $q \in \Pi$ and $\chi \in \mathring{W}_1^1(x_A,x_B)$. Here $\boldsymbol{E}\chi \in H^1(\Omega)$ denotes any extension of χ satisfying $\boldsymbol{E}\chi|_{\Gamma_D} = \boldsymbol{0}$ and $\boldsymbol{E}\chi\cdot\boldsymbol{n}|_{\Gamma_F} = \chi$.

It is not possible to have an extension operator $\boldsymbol{E}$ that maps $\mathring{W}_1^1(x_A,x_B)$ boundedly to $\boldsymbol{H}^1(\Omega)$ (see the example given by Saavedra & Scott (1991)). Thus (2.17) must be modified in some way to make it a rigorous basis for variational approximation

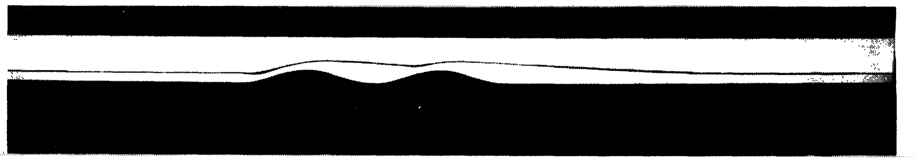

Figure 1. A photograph indicating the free-surface profile for flow at a Reynolds number of approximately 12. The flow is from right to left. The free surface of the liquid in the central portion of the channel is indicated by the lower edge of the thin line which derives from the meniscus on the side wall of the channel; the slight thickening of this line on the leeward side of the humps indicates the presence of some local structure near the side walls of the channel. The distance between the crests of the two humps in the channel bed is 100 mm.

methods. If we do not require that $\zeta \in W^1_\infty$, then Ω may cease to be a Lipschitz domain, leading to considerable technical complications. There is, however, an extension operator that maps $\mathring{W}^1_1(x_{\mathrm{A}}, x_{\mathrm{B}})$ boundedly to $\boldsymbol{W}^1_r(\Omega)$, provided that $r < 2$. Thus a possible modification is to replace V and Π by the spaces

$$V^r := \{\boldsymbol{v} \in \boldsymbol{W}^1_r(\Omega) : \boldsymbol{v} = 0 \text{ on } \Gamma_{\mathrm{D}}, \quad \boldsymbol{v} \cdot \boldsymbol{n} = 0 \text{ on } \Gamma_{\mathrm{F}}\},$$

$$\Pi^r := \left\{ q \in L^r(\Omega) : \int_\Omega q(\boldsymbol{x})\, \mathrm{d}\boldsymbol{x} = 0 \right\},$$

and to change the variational problem as follows.

Find $\boldsymbol{u}$ such that $\boldsymbol{u} - \boldsymbol{g} \in V^s$, $p \in \Pi^s$ and $\zeta - H \in \mathring{W}^1_\infty(x_{\mathrm{A}}, x_{\mathrm{B}})$ such that (2.17) holds for all $\boldsymbol{v} \in V^r$, for all $q \in \Pi^r$ and for all $\chi \in \mathring{W}^1_1(x_{\mathrm{A}}, x_{\mathrm{B}})$, where $1/r + 1/s = 1$, with $r < 2$.

A formulation similar to this has been proved to be well posed by Saavedra & Scott (1991) for a closely related scalar problem.

(*c*) *Lubrication approximation*

Shown in figure 1 is a photograph, representative of the experimental situation, from which it is seen that the flow is typified by a long slender sheet of liquid distorted slightly by the humps. At the smaller flow rates the liquid depth was of the order of 3 mm, whereas the peaks of the bumps were separated by 100 mm. This feature suggests that gradients along the channel should be significantly smaller than those normal to the channel bed, so that a classical lubrication approximation to the flow should work fairly well. It was of interest to us to see over what range of Reynolds numbers the lubrication approximation would hold up, thereby giving a feel for the conditions under which higher-order effects would begin to play a role in the dynamics of the flow. A similar kind of application of lubrication theory to viscous free-surface flows has been given by Moffatt (1977), Huppert (1982*a*, *b*), Johnson (1988) and Preziosi & Joseph (1988); Bechtel *et al.* (1988) have shown how to apply detailed lubrication-type expansions for free jets. Manton (1971) considered flow in a slowly varying pipe and developed a regular perturbation expansion (in terms of the maximum rate of change of the pipe diameter) to estimate the influence of inertial effects on the flow. We use a slightly different approach here.

To quantify the above ideas we introduce the (small) parameter ϵ defined by

$$\epsilon := \sup\{|b'(x)| : x_{\mathrm{A}} \leqslant x \leqslant x_{\mathrm{B}}\},$$

where x denotes distance along the plane. Let y be the coordinate normal to the plane and let $\boldsymbol{u} := (u, v)$ denote the velocity relative to this coordinate frame. We scale the

x variable, to reflect the slow variation along the plane, by introducing a new variable $X := \epsilon x$. (It will ensue that, for the experimental situation, the value of ϵ thus defined is about 0.3.) Central to the ideas of lubrication theory is the existence of a self-similar velocity field in y at each location along the channel. To this effect, we introduce a similarity variable $\eta\colon [b(\cdot),\ \zeta(\cdot)] \rightarrow [0,1]$, where

$$\eta := (y - b(\cdot))/(\zeta(\cdot) - b(\cdot)), \tag{2.18}$$

and it will be convenient to denote the thickness of the film by t, so that $t(X) := \zeta(X) - b(X)$. For steady flows the flux Q down the plane is given by

$$Q := \int_{b(\cdot)}^{\zeta(\cdot)} u(\cdot, y)\,\mathrm{d}y = \int_0^1 t(\cdot)\,u(\cdot,\eta)\,\mathrm{d}\eta. \tag{2.19}$$

Because of the asymptotic structure of the flow far upstream of the humps, it is convenient to use the flux Q and the asymptotic depth H as the basic scales, in which case we assign $Q = 1$ and $H = 1$ for the present analysis. Equation (2.19) suggests a new variable for the velocity along the plane, a kind of depth-averaged velocity, namely

$$U(X,\eta) := t(X)\,u(X,\eta), \tag{2.20}$$

so that

$$\int_0^1 U(\cdot,\eta)\,\mathrm{d}\eta = 1. \tag{2.21}$$

The above definitions can be used to develop an approximation to the Stokes equations which, formally, is valid to $O(\epsilon)$. We shall, however, be interested in allowing for small inertial corrections which, it is anticipated, will accumulate over lengths of $O((\epsilon R)^{-1})$. Thus we can expect the self-similar velocity field that arises in classical lubrication theory to be modified on the slow scale $\xi := \epsilon R X (= \epsilon^2 R x)$. The introduction of this new variable implies that we should, in fact, consider $U = U(X, \eta(X,y,\xi), \xi(X))$ and, correspondingly, the thickness $t = t(X,\xi)$. In terms of these new independent variables it follows that

$$\partial u/\partial x = -\epsilon t^{-2}\{-tU_X + Ut_X + (b' + \eta t_X)\,U_\eta + \epsilon R[\eta U_\eta t_\xi + Ut_\xi - tU_\xi]\}, \tag{2.22}$$

so that the velocity v normal to the plane can be determined from the divergence condition (2.2) as

$$v(X,\eta,\xi) = \epsilon t^{-1}\int_0^\eta \{t_X U + [b' + z t_X]\,U_z(X,z,\xi)\}\,\mathrm{d}z - \epsilon\int_0^\eta U_X(X,z,\xi)\,\mathrm{d}z + O(\epsilon^2 R). \tag{2.23}$$

After an integration by parts, (2.23) resolves as

$$v(X,\eta,\xi) = \epsilon t^{-1}[b'(X) + \eta t_X]\,U(X,\eta,\xi) - \epsilon\int_0^\eta U_X(\cdot,z,\cdot)\,\mathrm{d}z + O(\epsilon^2 R). \tag{2.24}$$

We note, in passing, that $v = O(\epsilon)$ and that, in view of (2.21), $v(X,1,\xi) = \epsilon\zeta_X u$, to the same order of approximation, as must be the case.

The y-momentum equation (cf. (2.1)) shows that

$$\partial p/\partial y + G\cos\alpha = O(\epsilon, R\epsilon^2), \tag{2.25}$$

from which it follows that

$$p(X,y,\xi) = p(X,\zeta(X),\xi(X)) + G\cos\alpha(\zeta(X) - y) + O(\epsilon, R\epsilon^2), \tag{2.26}$$

where $p(X, \zeta(X), \xi(X))$ is the pressure at the free surface. Then, a direct substitution in the x-momentum equation (cf. (2.1)) shows that

$$-\epsilon R t^{-3} t_X U^2 + \epsilon R t^{-2}\left(UU_X + U_\eta \int_0^\eta U_X(\cdot, z, \cdot)\,\mathrm{d}z\right) = -\epsilon p_X + t^{-3} U_{\eta\eta}(X, \eta) + G \sin\alpha, \tag{2.27}$$

which equation holds formally to $O(\epsilon^2, \epsilon^2 R)$.

The limit equation for $R = 0$, i.e. the ξ-independent equation, is thus seen to be

$$t^{-3}(X)\, U_{\eta\eta}(X, \eta) = \epsilon p_X - G \sin\alpha, \tag{2.28}$$

and the limit equation for $\epsilon = 0$, corresponding to flow down a uniform plane, is

$$t^{-3}(X)\, U_{\eta\eta}(X, \eta) = -G \sin\alpha. \tag{2.29}$$

The scaling for the flow is such that $t(0) = 1$. Equation (2.29) is subject to the no-slip condition $U(X, 0) = 0$ on the plane, and to the condition $U_\eta(X, 1) = 0$ at the free surface, corresponding to the shear stress vanishing there, and therefore has the solution

$$U(0, \eta) = \tfrac{1}{2} G\,(2\eta - \eta^2) \sin\alpha, \tag{2.30}$$

and, as a consequence of the flux condition (2.21), it follows that

$$1 = \tfrac{1}{3} G \sin\alpha. \tag{2.31}$$

Equations (2.30) and (2.31) correspond to the classic Poiseuille–Nusselt solution for flow down a uniform plane.

Returning now to the problem with ϵ non-zero, but keeping $R = 0$, we have to find a velocity field U and a pressure field p satisfying (2.28) together with the appropriate boundary conditions for the flow. The no-slip condition on the bed of the channel implies that $U(X, 0) = 0$. It is easily checked that the zero shear-stress condition (2.6) at the free surface is satisfied to $O(\epsilon^2)$ by the specification that $U_\eta(X, 1) = 0$. The normal-stress condition (2.7) at the free surface $y = \zeta(X)$ can now be evaluated and the unknown function $p(X, \zeta(X))$ fixed. A simple calculation shows that

$$p(X, \zeta(X)) = -\epsilon^2 S \zeta''(X) + O(\epsilon, S\epsilon^4), \tag{2.32}$$

and the pressure gradient in (2.28) can now be expressed in terms of the other variables to yield

$$U_{\eta\eta}(X, \eta) = t^3(X)\,(-\epsilon^3 S \zeta'''(X) + 3\epsilon\, \zeta'(X) \cot\alpha - 3), \tag{2.33}$$

which equation is to be solved subject to

$$U(\cdot, 0) = 0, \quad U_\eta(\cdot, 1) = 0 \quad \text{and} \quad \int_0^1 U(\cdot, \eta)\,\mathrm{d}\eta = 1. \tag{2.34}$$

Equation (2.33) together with (2.34) poses a slightly unusual problem in that, for a given X, the two-point boundary-value problem for U gives the basic form for the velocity field, but, because of the unknown surface height ζ, the scale of U has to be fixed by the continuity condition, expressed by the integral constraint in (2.34). This is merely an alternative expression of the usual bootstrap argument made in conventional lubrication theory in a fixed domain, in which the pressure field is determined from the divergence condition, once the basic velocity field is known. Indeed, the lubrication approximation embodied in (2.33) and (2.34) shows clearly the separation of variables X and η, as used in classical lubrication theory, which separation is enabled because of the linearity of the momentum equation when $R = 0$. Thus, we see from (2.33) and (2.34) that the velocity field $U(X, \eta)$ is quadratic in η and depends on the slow scale X according to

$$\epsilon^3 S\zeta'''(X) - 3\epsilon\,\zeta'(X)\cot\alpha - 3[\zeta(X) - b(X)]^{-3} = -3. \tag{2.35}$$

The special case with $S = 0$ yields the standard lubrication approximation (cf. Huppert 1982*a*)

$$\zeta'(x) = \tan\alpha(1 - 1/(\zeta(x) - b(x))^3), \tag{2.36}$$

which we shall henceforth refer to as the LX model.

The asymptotic states far upstream and downstream require, with $b = 0$, that $\zeta \rightarrow 1$ smoothly as $x \rightarrow \pm\infty$. Thus, the condition $\zeta = 1$ can be used to start the integration of (2.36). This integration must proceed upstream, as the downstream integration can easily be shown to be unstable. The boundary conditions $\zeta(\pm\infty) = 1$ and $\zeta'(\infty) = 0$ are appropriate for the third-order problem (2.35), in that they provide a well-posed problem for the linearized version of the equation. In the results to be described below in §4, numerical solutions to (2.35) were found by using the ordinary differential equation package COLNEW (see Ascher *et al.* 1988) which employs a collocation method and a Newton procedure to solve the two-point boundary value problem.

We can now address the problem for non-zero, but small, Reynolds numbers as expressed by (2.27). In view of (2.35) it follows that $U_X(X, \eta, \xi) = O(\epsilon R)$, so that the terms involving U_X on the left-hand side of (2.27) are seen to be of $O((\epsilon R)^2)$, and the equation resolves as

$$U_{\eta\eta}(X, \eta) + \epsilon R t'(X)\, U^2(\eta) = t^3(X)\,(-\epsilon^3 S\zeta'''(X) + 3\epsilon\,\zeta'(X)\cot\alpha - 3), \tag{2.37}$$

to be solved subject to the conditions (2.34). Note that in (2.37) we have omitted the dependence on ξ as it does not appear explicitly at this level of approximation.

(i) *Solution procedure*

To solve (2.37) in the general case with $R \neq 0$ we consider the two-point boundary-value problem for the function W: $[0, 1] \rightarrow \mathbb{R}$, such that

$$W''(\eta) + rW^2(\eta) = -f, \tag{2.38a}$$

subject to

$$W(0) = 0 \quad \text{and} \quad W'(1) = 0, \tag{2.38b}$$

where

$$r(X) := \epsilon R t'(X), \quad \text{and} \quad f(X) := t^3(X)\{\epsilon^3 S\zeta'''(X) - 3\epsilon\cot\alpha\,\zeta'(X) + 3\}. \tag{2.39}$$

The difficulty in solving the problem at hand is that of finding particular values for the functions r and f such that the solution W to (2.38*a* and *b*) satisfies the flux constraint. Suppose, therefore, that r and f take some given values and let W be the solution to (2.38*a*, *b*), with r, f thus specified. Define a flux $Q(r, f)$ as

$$Q(r, f) := \int_0^1 W(y)\,\mathrm{d}y, \tag{2.40}$$

and the goal is to find appropriate choices of r and f, for each X, such that $Q = 1$, in keeping with (2.34). Note that the existence of a solution to (2.38*a*, *b*), when $r < r_0$, for some $r_0 > 0$, follows directly from standard variational theory.

To satisfy the constraint (2.40) it is convenient, by virtue of the implicit function theorem, to write f as a function of r and determine $f(r)$ such that $Q(r, f(r)) = 1$. (Such an elimination is possible up to a value of r of approximately 5.46, at which point our computations indicate there is a simple turning point in the graph of $f(r)$.) A Taylor series approximation to $f(r)$ can readily be obtained in the neighbourhood of $r = 0$. Note that, at $r = 0$, (2.38a) is linear, so that $Q(0, f) = fQ(0, 1)$ and, since $W(\eta) = f\eta(1-\frac{1}{2}\eta)$, it follows that $Q(0, 1) = \frac{1}{3}$, and so $f(0) = 3$. A relatively straightforward calculation shows $f'(0) = -\frac{54}{35}$, and higher-order terms can readily be computed. The linear approximation to f is thus seen to be

$$f_1(r) = 3 - \tfrac{54}{35}r. \tag{2.41}$$

(The linear approximation to $f(r)$ near $r = 0$ can be determined as follows. Since the flux Q is a constant, it follows from (2.40) that $f'(0) = -Q_r(0, f(0))/Q_f(0, f(0))$, so that $f'(0) = -3Q_r(0, f(0))$. The determination of Q_r must, of course, be related to the solution $W(\eta; r, f)$ of the differential equation (2.38) for given r and f. We therefore need to consider the limit as $r \rightarrow 0$ of the difference

$$V(\eta; r, f) := \{[W(\eta; r, f) - W(\eta; 0, f)]/r\},$$

with f held fixed, which limit, namely $V(\eta; 0, f)$, is given, by use of (2.38), as the solution of $V_{\eta\eta}(\eta; 0, f) = -W^2(\eta; 0, f)$, subject to $V(0; 0, f) = V_\eta(1; 0, f) = 0$. Thus, $V(\eta; 0, f)$ can be found by direct integration, and a further integration allows the desired result to be calculated.)

(ii) *A hierarchy of models*

Although it is feasible to calculate analytically more terms in the Taylor expansion of f, we have instead chosen to compute (2.38) numerically, using a difference approximation of the kind attributed variously to Stömer (Whittaker & Robinson 1944) and to Numerov (see Kopal 1955). Consider a uniform mesh of size $\Delta\eta$ on $[0, 1]$ and let $N := 1/\Delta\eta$. We approximate the differential equation (2.38a) by

$$D_2 W = (I - \tfrac{1}{12}(\Delta\eta)^2 D_2)(f + rW^2), \tag{2.42}$$

where D_2 denotes a centred second-difference operator (i.e. D_2 corresponds to the $N \times N$ tri-diagonal matrix with diagonal entries equal to $2/(\Delta\eta)^2$ and off-diagonal entries equal to $-1/(\Delta\eta)^2$, except for the entry $(D_2)_{N,N-1}$ which equals $-2/(\Delta\eta)^2$, because of the Neumann boundary condition to be satisfied at $\eta = 1$.) The modification to the identity matrix, I, on the right-hand side of (2.42) makes the system a fourth-order accurate representation of (2.38).

The integral (2.40) has been discretized using a modification to the trapezoidal rule based on the Gregory and the Euler–Maclaurin formulae. Thus we replace the integral by

$$\Delta\eta \sum_{i=1}^{N} c_i W_i,$$

where $c_i = 1$, with the exceptions

$$c_1 = \tfrac{7}{6}, \quad c_2 = \tfrac{23}{24} \quad \text{and} \quad c_N = \tfrac{1}{2}.$$

The above discretization is an approximation to the Euler–Maclaurin formula in which fourth-order accurate corrections are made at the ends of the interval. At the left-hand end the derivative-correction term is approximated by a second-order

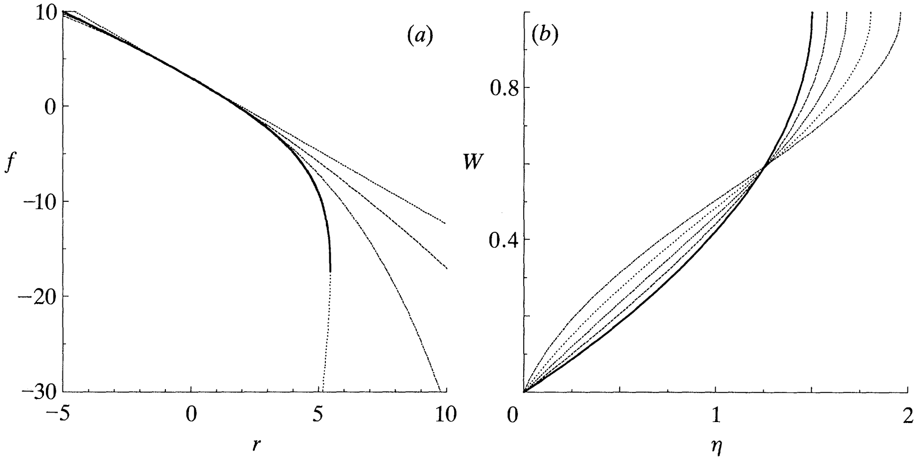

Figure 2. (*a*) A graph of the function $f(r)$ defined by (2.38) together with the first (----), second (– – –) and fourth (–·–) order Taylor approximation to f about (0, 3). Note that f has a turning point at $r \approx 5.4515$ and the continuation of f beyond that turning point is indicated by the dotted curve. (*b*) The velocity distribution $W(\eta)$, showing how it is modified by nonlinear effects. (——), $r = 0$, $f = 3$; (– – –), $r = 1.241$, $f = 1$; (----), $r = 2.349$, $f = -1$; (······), $r = 3.292$, $f = -3$; (–·–), $r = 4.043$, $f = -5$.

difference operator, thus retaining fourth-order accuracy, and use is made of the fact that $W(0) = 0$. At the right-hand end of the interval, use is made of the boundary condition $W'(1) = 0$.

The discrete approximation to (2.38) and (2.40) can now be expressed as

$$F(W, f, r) = 0,$$

where F represents the following $N+1$ expressions

$$\begin{pmatrix} (I - \tfrac{1}{12}(\Delta\eta)^2 D_2)^{-1} D_2\, W - rW^2 - f \\ N - c^t W \end{pmatrix}.$$

Since F depends on $N+2$ variables, we can choose one of the variables, r say, to be the independent variable and solve for W and f (e.g. by Newton's method). Since the only nonlinearity in F is the quadratic term, $W^2 := (W_i^2)$, the jacobian of F is easily computed as

$$J_{\mathrm{F}}(W, f) = \begin{pmatrix} (I - \tfrac{1}{12}(\Delta\eta)^2 D_2)^{-1} D_2 - 2rL(W) & -E \\ -c^t & 0 \end{pmatrix}, \tag{2.43}$$

where E denotes the (column) vector of all ones and $L(W)$ denotes the diagonal matrix whose ith diagonal entry is equal to W_i. Note that our scaling makes the jacobian very nearly symmetrical.

Using these techniques, we have computed $f(r)$ to be shown as in figure 2. Also shown in figure 2 are some approximations to f obtained from various orders of the Taylor expansion of f about $r = 0$. These approximations are defined by $f_k(r)$ where

$$f_k(r) := \sum_{l=0}^{k} f^{(l)}(0) r^l, \tag{2.44}$$

and we consider only the cases $k = 0, 1, 2, 4$. The coefficients $f^{(l)}(0)$ have been determined as: $f^{(0)}(0) = 3, f^{(1)}(0) = -\frac{54}{35}, f^{(2)}(0) \approx -0.046\,308$, $f^{(3)}(0) \approx -0.006\,087$, and $f^{(4)}(0) \approx -0.000\,871$, with the latter three coefficients having been found by numerical computation. Each of the approximations $f_k(r)$ defined by (2.44) can be used to provide a lubrication model in its own right. These take the form

$$\epsilon^3 S \zeta'''(X) - 3\epsilon\zeta'(X)\cot\alpha - f_k(r)\,[\zeta(X) - b(X)]^{-3} = -3. \qquad (2.45)$$

We have restricted our numerical experiments to the cases $k = 0$ (the improved lubrication approximation (2.35)), $k = 1$, $k = 2$, $k = 4$ and the exact representation of f, which models we shall refer to respectively as L0, L1, L2, L4 and L∞. Interesting differences have been found in the computations described in §4 between the solutions of the various models defined by (2.45) and the finite element computations based on the complete problem.

The differential equation (2.45) has been solved using the aforementioned package COLNEW, subject to the boundary conditions $\zeta(\pm\infty) = 1, \zeta'(-\infty) = 0$. It was, however, found that solutions to the models L1, L2, L4 and L∞ were not possible above a certain value of R. The reasons for this are not completely understood by us, but an indication of why there might not be a solution as R increases is given by rewriting (2.45) in terms of the film thickness $t(X)$. Thus, for the case $k = 1$, we find that (2.45) takes the form

$$\epsilon^3 S t'''(X) - \epsilon(3\cot\alpha - \tfrac{54}{35} R t^{-3}(X))\, t'(X) = -3 + 3\epsilon\, b'(X)\cot\alpha - \epsilon^3 S b'''(X), \qquad (2.46)$$

for which $t(\pm\infty) = 1$ and $t'(-\infty) = 0$, and note that b and all its derivatives vanish at $\pm\infty$. (Because the length scale used here is based on the upstream depth, the function b and the variable X depend implicitly on the flow rate and hence on R. Thus, the term involving b''' in (2.46) depends implicitly on R, whereas the other terms on the right-hand side of (2.46) are independent of R.) When $S = 0$, (2.46) reduces to a first-order equation and we see that t will fail to be differentiable should the thickness t reach the critical value

$$t_1^* = (18R/35\cot\alpha)^{\frac{1}{3}}. \qquad (2.47)$$

It has been found numerically, when simulating the experimental conditions to be described below, that smooth solutions to (2.45), for the case with $S = 0$, were not possible for values of R exceeding 5.1, 5.1, 5.1, and 2.5 for the respective models L1, L2, L4, and L∞. In these experiments, the breakdown of the L1-model occurred at a film thickness in very close agreement with the value 0.336 for t_1^* given by (2.47).

With S not equal to zero (in fact $S \approx 18R^{-\frac{2}{3}}$ in our experiments), the range of Reynolds numbers over which smooth solutions were obtainable was increased to 15, 9.4, 7.7, 8.0, for the respective models. The maximum values of r, and the corresponding value of f, associated with these critical Reynolds numbers were: 18.5, -25.5 (model L1); 6.90, -9.84 (model L2); 4.02, -5.34 (model L4) and 4.31, -5.90 (model L∞).

Some examples are given in figure 2*b* of the modification induced by the nonlinear term $\epsilon R t' U^2$ to the basic Poiseuille–Nusselt profile. Note that the curve for W at $r = 4.043$ shown here was near the largest value of r for which solutions to (2.45) were obtainable for the L∞ model.

(*d*) *Numerical algorithms*

Discrete methods for the Navier–Stokes problem (2.1) and (2.2), subject to boundary conditions (2.4)–(2.6) on a fixed domain Ω, can be obtained through the variational formulation (2.8) by choosing discrete subspaces $V_h \subset V$ and $\Pi_h \subset \Pi$, where the parameter h denotes the accuracy of the discretization. Assume, for the time being, that Ω has a polygonal boundary. Two pairs of spaces that are known theoretically (see Brezzi & Falk 1992) to lead to convergent methods are as follows. Suppose that a triangulation, $\mathscr{T}_h$, of the domain Ω is given. Define h (see (4.2) below) to be the square root of the ratio of the maximum area of any triangle in $\mathscr{T}_h$ to the area of Ω, and thus $0 < h \leqslant 1$. We shall assume that the points of intersection of the domains Γ_{F} and Γ_{D} are vertices in $\mathscr{T}_h$. Let $\mathscr{P}_n$ denote polynomials of degree n or less in two variables. Then define

$$V_h := \{\boldsymbol{v} \in V : (v_1, v_2)|_\tau \in \mathscr{P}_2, \forall \tau \in \mathscr{T}_h\}, \tag{2.48 v}$$

$$\Pi_h := \{q \in \Pi \cap C^0(\Omega) : q|_\tau \in \mathscr{P}_1, \forall \tau \in \mathscr{T}_h\}. \tag{2.48 p}$$

For piecewise polynomials, the condition $\boldsymbol{v} \in V$ is equivalent to the condition that each component, v_i, be continuous. However, the restriction $q \in \Pi$ places no continuity restriction on a piecewise polynomial, q. Specifically, the method of this class to be used in the numerical computations is the one first introduced by Taylor & Hood (1973) for which the velocity field is comprised of polynomials that are piecewise quadratic on each triangle and have C^0-continuity on the domain Ω; the pressure field is comprised of functions that are piecewise linear on each triangle and have C^0-continuity on Ω. We refer to this method as the QLT method, denoting the quadratic and linear approximations to the velocity and pressure fields on each triangle.

Similarly, let $\mathscr{F}_h$ denote a subdivision of Ω into quadrilaterals. We again define h to be the square root of the ratio of the maximum area of any quadrilateral in the subdivision to the area of Ω, and let $\mathscr{Q}_2$ denote biquadratic polynomials (products of polynomials of degree 2 or less in each variable separately). For a given quadrilateral, $\varpi \in \mathscr{F}_h$, let β_ϖ denote a bilinear mapping of a translate of $[0,1] \times [0,1]$ to ϖ. Then define

$$V_h := \{\boldsymbol{v} \in V : v_i \circ \beta_\varpi|_{[0,1]\times[0,1]} \in \mathscr{Q}_2, \forall \varpi \in \mathscr{F}_h \quad \text{and} \quad i = 1, 2\}, \tag{2.49 v}$$

$$\Pi_h := \{q \in \Pi : q|_\varpi \in \mathscr{P}_1, \forall \varpi \in \mathscr{F}_h\}. \tag{2.49 p}$$

The specific method of this class to be used here is the one analysed by Bercovier & Engleman (1979). In this case the velocity field is comprised of biquadratic polynomials on each quadrilateral and which have C^0-continuity on Ω; the pressure field is comprised of polynomials that are piecewise linear on each quadrilateral but do not have any continuity constraints between quadrilaterals. We refer to this method as the BQLQ method, denoting the biquadratic and linear approximations on each quadrilateral.

Should the Dirichlet data, $\boldsymbol{g}$, not be representable by a piecewise polynomial of the appropriate degree, then typically the boundary data $\boldsymbol{g}$ are represented by an interpolant, $\mathscr{I}_h \boldsymbol{g}$, as shown, for example, in Ciarlet (1978). Here we take $\mathscr{I}_h$ to be the standard Lagrange interpolant.

When the continuous problem has a unique solution it is known (see Girault & Raviart 1986; Brezzi & Falk 1991) that, using either the pair of spaces (2.48) or the pair (2.49), the following discrete problem has a unique solution, for h sufficiently small.

Find $\boldsymbol{u}_h$, such that $\boldsymbol{u}_h - \mathscr{I}_h \boldsymbol{g} \in V_h$, and $p_h \in \Pi_h$ such that

$$\left.\begin{aligned} a(\boldsymbol{u}_h, \boldsymbol{v}) + d(\boldsymbol{v}, p_h) &= Rc(\boldsymbol{u}_h, \boldsymbol{u}_h, \boldsymbol{v}) + G\int_\Omega \boldsymbol{j} \cdot \boldsymbol{v} \, \mathrm{d}\boldsymbol{x}, \quad \forall \boldsymbol{v} \in V_h, \\ d(\boldsymbol{u}_h, q) &= 0, \quad \forall q \in \Pi_h. \end{aligned}\right\} \tag{2.50}$$

Then
$$\|\boldsymbol{u}-\boldsymbol{u}_h\|_{H^1(\Omega)}+\|p-p_h\|_{L^2(\Omega)} \leqslant Ch^2(\|\boldsymbol{u}\|_{H^3(\Omega)}+\|p\|_{H^2(\Omega)}), \tag{2.51}$$
where C is a constant which depends only on Ω, R, G and the smallest angle made by any pair of adjacent edges in $\mathscr{T}_h$ or $\mathscr{F}_h$. Estimates based on closely related scalar elliptic problems (see, for example, Ciarlet 1978; Duran *et al.* 1988) suggest that it should be possible in the present case to show that, not only do the discrete schemes satisfy (2.51), but that the errors also satisfy
$$\|\boldsymbol{u}-\boldsymbol{u}_h\|_{L^r(\Omega)}+h\|p-p_h\|_{L^r(\Omega)} \leqslant Ch^3(\|\boldsymbol{u}\|_{W^3_r(\Omega)}+\|p\|_{W^2_r(\Omega)}), \quad 1\leqslant r\leqslant\infty. \tag{2.52}$$

(i) *Procedures for testing numerical codes*

When a complex computer code is to be used in a scientific investigation, especially one not written by the users of the code, it is crucial that a careful assessment be made of it to determine whether the intended algorithms have been correctly implemented and to ascertain the limitations of the code. It is not usually a completely straightforward exercise to assess a practical code in terms of an estimate such as that given in (2.52). There are several reasons for this: usually it is not easy to come up with an exact solution $\{\boldsymbol{u}, p\}$ on a relatively complicated domain; or, even if an exact solution is known (or is computed by some auxiliary means, as is done subsequently for the Jeffery–Hamel flow), it is not feasible to compute exactly the Lebesgue norms, $L^r(\Omega)$, of the errors, unless the exact solution is particularly simple. This can be avoided by substituting for the exact solution an interpolant. (This technique also simplifies comparison with experimental data as well.) For the spaces (2.48) and (2.49), the standard Lagrange interpolant (see Ciarlet 1978) satisfies
$$\|\boldsymbol{u}-\mathscr{I}_h\boldsymbol{u}\|_{L^r(\Omega)}+h\|p-\mathscr{I}_h p\|_{L^r(\Omega)} \leqslant Ch^3(\|\boldsymbol{u}\|_{W^3_r(\Omega)}+\|p\|_{W^2_r(\Omega)}), \quad 1\leqslant r\leqslant\infty. \tag{2.53}$$
From the triangle inequality, the validity of an estimate of the form (2.52) would then imply that
$$\|\mathscr{I}_h\boldsymbol{u}-\boldsymbol{u}_h\|_{L^r(\Omega)}+h\|\mathscr{I}_h p-p_h\|_{L^r(\Omega)} \leqslant Ch^3(\|\boldsymbol{u}\|_{W^3_r(\Omega)}+\|p\|_{W^2_r(\Omega)}), \quad 1\leqslant r\leqslant\infty. \tag{2.54}$$
While it is possible to compute the norms on the left-hand side of (2.54) for some values of r, it is useful to make a further simplification as follows. For an element τ of $\mathscr{D}_h$, let Σ_τ denote the appropriate Lagrange interpolation points for a given space of polynomials $\mathscr{P}(=\mathscr{P}_1, \mathscr{P}_2$ or $\mathscr{Q}_2$ in the present context). Let
$$H_\tau(v) := |\tau| \sum_{x\in\Sigma_\tau} v(x), \tag{2.55}$$
where $|\tau|$ denotes the area of τ. Then there is a positive constant, C, depending only on the smallest angle in τ such that
$$\frac{1}{C}\int_\tau |v(x)|^r\,\mathrm{d}x \leqslant H_\tau(|v|^r) \leqslant C\int_\tau |v(x)|^r\,\mathrm{d}x,$$
for every $v\in\mathscr{P}$. Thus, if we define
$$E_r(v) := \left(\sum_{\tau\in\mathscr{D}_h} H_\tau(|v|^r)\right)^{1/r}, \tag{2.56}$$
(with the obvious corresponding extension for vector-valued functions), it follows

that there is a constant, C, depending only on the smallest angle in $\mathscr{D}_h$, such that, for $1 \leqslant r < \infty$,

$$(1/C)\,\|v\|_{L^r(\Omega)} \leqslant E_r(v) \leqslant C\|v\|_{L^r(\Omega)}, \tag{2.57}$$

for all piecewise-polynomial functions under consideration. A similar argument extends the validity of (2.57) to the case $r = \infty$, where $E_\infty(v)$ is defined to be the maximum of $|v|$ at all the Lagrange interpolation points, Σ_τ, for every $\tau \in \mathscr{D}_h$. The validity of (2.52) would then imply that

$$E_r(\mathscr{I}_h\boldsymbol{u} - \boldsymbol{u}_h) + hE_r(\mathscr{I}_h p - p_h) \leqslant Ch^3(\|\boldsymbol{u}\|_{W^3_r(\Omega)} + \|p\|_{W^2_r(\Omega)}), \quad 1 \leqslant r \leqslant \infty. \tag{2.58}$$

If an exact solution $(\boldsymbol{u}, p)$ is known, it is a relatively simple matter to compute the expression on the left-hand side of (2.58) to determine whether or not the functions provided by a code satisfy (2.58) asymptotically as the mesh size, h, is reduced. Tests of this sort will be presented subsequently.

(ii) *Variational formulation of the free-boundary problem*

A variational formulation, based on (2.17), for the free-boundary problem (2.1)–(2.7) requires the introduction of a space $S_h \subset \mathring{W}^1_\infty(x_A, x_B)$ for the approximation of ζ. A natural space to complement (2.48) and (2.49) is the set of all piecewise-quadratic functions on a subdivision of $[x_A, x_B]$. It is convenient for computational purposes to link the meshes used for the boundary approximation space, S_h, and the mesh, $\mathscr{D}_h$, used for the interior approximation spaces, (2.48) or (2.49). Moreover, the interior mesh must be allowed to depend on the discrete approximation of the free-boundary, ζ_h. This can be done in the following way. Suppose that we start with a fixed mesh, $\mathscr{D}^0_h$, on the domain Ω^0 corresponding to some initial guess for the free surface, ζ^0, say. We require that the vertices of the mesh for S_h coincide with the x-coordinates for the vertices of $\mathscr{D}_h$ on the prescribed initial surface at $y = \zeta^0$. In the simplest case, we define a new mesh, $\mathscr{D}^\zeta_h$, depending on $\zeta \in S_h$ through the coordinate mapping

$$\boldsymbol{x} \rightarrow (x, (\zeta(x)/H)\,y), \tag{2.59}$$

which simply stretches or contracts the mesh in the vertical direction to match the required surface height, $\zeta(x)$. More complicated mappings are also possible, as will be discussed subsequently.

Using a mapping such as that introduced in (2.59), it is possible (see Ciarlet 1978) to introduce new discrete spaces $V^{\zeta_h}_h$ and $\Pi^{\zeta_h}_h$ as isoparametric images of V_h and Π_h defined on $\mathscr{D}^0_h$. The discrete approximation for the problem defined by (2.1)–(2.7) is then:

find $\zeta_h - H \in S_h, \boldsymbol{u}_h$ such that $\boldsymbol{u}_h - \mathscr{I}_h\boldsymbol{g} \in V^{\zeta_h}_h$ and $p_h \in \Pi^{\zeta_h}_h$ such that

$$\left.\begin{aligned} \phi(\boldsymbol{u}_h, p_h, \boldsymbol{v}) &= 0, \\ d(\boldsymbol{u}_h, q) &= 0, \\ A(\zeta_h, \chi) &= \phi(\boldsymbol{u}_h, p_h, \boldsymbol{E}_h\,\chi), \end{aligned}\right\} \tag{2.60}$$

for all $\boldsymbol{v} \in V^{\zeta_h}_h$, $q \in \Pi^{\zeta_h}_h$ and $\chi \in S_h$.

Here $\boldsymbol{E}_h\,\chi$ denotes any extension of χ such that $\boldsymbol{E}_h\,\chi \cdot \boldsymbol{n}|_{\Gamma_F} = \chi$. As in the continuous case, the solution to (2.60) is independent of the choice of the extension.

There is no error analysis currently available for (2.60). However, once the solution ζ_h is known, the first two equations of (2.60) imply that $(\boldsymbol{u}_h, p)$ may be thought of as solving a fixed-domain problem on the domain, Ω_h. Should this domain be close to

Ω, we can apply the triangle inequality together with (2.51), to deduce the accuracy of the method. Note that the estimate (2.51) has not been proved for isoparametric elements based on (2.48) and (2.49), but results obtained from the closely related scalar case (Ciarlet 1978) suggest that it is not unreasonable to presume the validity of (2.51) as a working hypothesis. Since the free-surface is here approximated by piecewise quadratic functions, it is therefore expected that

$$\|\zeta-\zeta_h\|_{L^r(\Omega)} \leqslant Ch^3\|\zeta\|_{W^3_r(\Omega)}, \quad 1 \leqslant r \leqslant \infty. \tag{2.61}$$

(iii) *Solution of the nonlinear equations*

The set of equations (2.60) represent $N := \dim V_h + \dim \Pi_h + \dim S_h$ equations in N unknowns. They can be written in a more familiar form simply by replacing $\boldsymbol{v}, q, \chi$ by members of bases of the spaces V_h, Π_h, S_h, for which the resultant system of equations may be solved by a variety of techniques, including Newton's method. We also note that there is a special fixed-point iteration similar to the theoretical argument used by Jean (1980) and by Solonnikov (1980) in which the first two equations of (2.60) are solved for fixed ζ_h, and then the third equation is solved using the newly computed $\boldsymbol{u}_h, p_h$ to provide an updated ζ_h, and the process is repeated. For R not too large and S not too small, this essentially decouples the free-boundary problem into two (nearly) linear problems on fixed domains.

When a range of values of R is to be analysed, it is natural to use a 'continuation' method, in which previous solutions at smaller values of R are used as the first guess (including the initial guess for the domain) at the beginning of an iterative technique used to solve (2.60). Another, more unusual, technique for solving such problems is to introduce an artificial parameter, $0 \leqslant \omega \leqslant 1$, and solve with a bed of elevation $\omega b(x)$, beginning at $\omega = 0$ for which the solution of the free-surface problem is known explicitly, and continuing until $\omega = 1$ is reached. As will be discussed subsequently, both continuation techniques were needed to compute the solution to the free-boundary problem corresponding to the physical experiments.

(*e*) *Implementation of numerical methods*

All the numerical solutions described herein to the problem posed by (2.1)–(2.7) were obtained by using the commercially available, finite-element package FIDAP (available from Fluid Dynamics International Inc., and see Engelman (1982)). This code offers a wide range of options, especially with regard to the choice of elements available for the representation of the dependent variables. We have, however, chosen to work with two of the more commonly used methods, for which the theoretical underpinning is as described above in §2*d*.

With the implementation made in FIDAP, the six nodes representing the velocity field in the QLT method (cf. §2*d*) are located at the triangle vertices and the triangle edge midpoints; the nodes for the (C^0) pressure field are located at the triangle vertices. The evaluation of the coefficients in the finite-element equations is effected by a seven-point numerical quadrature scheme. For the BQLQ method, the degrees of freedom associated with the (biquadratic) velocity approximation are located at the corners and edge mid-points and at the barycentre of the quadrilateral; the three degrees of freedom associated with the discontinuous, linear pressure approximation are fixed at the barycentre of the quadrilateral. Gaussian formulae are used to evaluate the coefficients associated with the finite-element equations. Isoparametric elements are used in both cases. Note that, in the present computations, the pressure is solved for directly as one of the independent variables: FIDAP allows for the possibility of resolving the divergence constraint by the use of a penalty formulation, but the method does not work well for free-surface flows.

(i) *Linear algebra*

The linear system to be solved is not symmetric, but it is sparse and banded. The solution is performed in FIDAP by direct gaussian elimination without pivoting and, should a pivot smaller than 10^{-8} be encountered, it is simply replaced by 10^{-8}. Small pivots were a very common occurrence in our computations and, since the procedure used by FIDAP solves a linear system modified from the original, some understanding of the effect of replacing pivots is needed. (We report below on some convergence studies in which the system was modified in this way.) The global matrix is stored in skyline form (see Hasbani & Engelman 1979) and the program has an option (invoked by calling `RENUMBER(PROFILE)` in the code) for nodal renumbering to minimize the number of storage locations in the skyline envelope. Use of the renumbering procedure gave large reductions in the solution times.

(ii) *Nonlinear algebra*

For the solution of steady free-surface flows FIDAP uses a Newton iteration scheme proposed by Saito & Scriven (1981). To provide some control on the way the free surface is adjusted at each stage of the iteration, and thereby help avoid possible unwanted singular or nearly singular jacobian matrices, the nodel points used in the discretization of the free surface are constrained to move along so-called spines (cf. §4*a*). These spines are a collection of straight lines which pierce the 'free surface' and which are assumed to intersect only outside the 'flow' domain, at each stage of the iteration. Thus the selection of the spines can be a matter for considerable care. Certain nodal points in the mesh are constrained to lie on the spines and are moved along the spines in proportion to the adjustment of the free surface. Nodes in between are adjusted by an interpolation procedure. Through the use of such spines, Saito & Scriven were able to calculate the jacobian for a class of free-surface flows of Navier–Stokes fluids, and showed computationally that the Newton iteration based on this jacobian did indeed converge at second order, as expected. In the calculations to be described below, the choice of the spines was relatively straightforward and is given in §4.

In our computations a number of strategies were used to provide the initial guess for the Newton iteration. One method used continuation in the Reynolds number, starting from the solution at $R = 0$. The lubrication approximation (see §2*c*) was very helpful in providing an initial approximation for the free surface profile at small values of R, and this could be used to initiate the Newton method at Reynolds numbers up to about 5. Another method we used was to use a continuation method, starting from the flow down a uniform plane, and then gradually to increase the size of the perturbations to the channel bed until the solution with the desired bed profile had been achieved. The radius of convergence for the Newton iteration seemed to become quite small at values of R in excess of 20, and we were unable to find a solution at some of the larger Reynolds numbers obtaining in the physical experiments.

The stopping procedure in FIDAP for the Newton iteration is based on the satisfaction of a pair of convergence criteria. The first of these looks at successive iterates $\boldsymbol{u}_i$ of the solution vector $\boldsymbol{u}$ being sought such that the system of equations

$\boldsymbol{R}(\boldsymbol{u}) = \boldsymbol{0}$, for which $\boldsymbol{R}(\boldsymbol{u}_i)$ is referred to as the residual vector at the ith iteration. Thus it is required that the relative difference between successive iterates should become smaller than a specified value ϵ_1, i.e. that

$$\|\boldsymbol{u}_i - \boldsymbol{u}_{i-1}\| / \|\boldsymbol{u}_i\| < \epsilon_1,$$

where $\|\cdot\|$ denotes the maximum euclidean norm of the appropriate vector field. The second criterion is that the residual vector be reduced by an amount ϵ_2 such that

$$\|\boldsymbol{R}(\boldsymbol{u}_i)\| / \|\boldsymbol{R}(\boldsymbol{u}_0)\| < \epsilon_2,$$

where $\boldsymbol{u}_0$ denotes the initial guess. Typically we set $\epsilon_1 \approx 10^{-5}$ and $\epsilon_2 \approx 10^{-5}$ for the comparisons with the experimental data.

(iii) *Boundary conditions*

The boundary conditions relating to the flow domain corresponding to the experimental situation are discussed in some detail in §2*a*. A photograph of the flow domain at $R \approx 12$ is shown above in figure 1. Dirichlet conditions on the velocity field were imposed on the channel bed (specifically the no-slip condition) and at the upstream and downstream locations x_A and x_B, at which stations the heights H of the streams were also specified, as discussed in §§2*a* and *b*. In principle the surface slopes at x_A and x_B will adjust to the global flow constraints, in which case some tangential velocity components are needed to ensure kinematic compatibility of the flow field. Unfortunately it is not possible in FIDAP to meet these constraints but, because the flow had effectively achieved its uniform asymptotic state at both the upstream and the downstream extremities of the computational domain, these potential incompatibilities proved to cause no problems at all in our calculations. Through the use of the formulation given in §2*b*, the shear-stress condition (2.6) at the free surface resolves as a natural boundary condition, and satisfaction of the normal-stress condition (2.7) is an end product of the Newton iteration.

3. Experimental apparatus and technique

(*a*) *Experimental apparatus*

The apparatus used for the present experiments was basically the same as that used in the experiments described by Pritchard (1986), to which paper reference should be made for further descriptions of the equipment. The central part of the apparatus was an open channel of width 127 mm and depth 74.5 mm, sloping at an angle of 0.0735 rad to the horizontal; it was 1.20 m long. At the upstream end of the channel was an inlet reservoir from which the liquid (an oil) poured into the channel and at the downstream end was a receiving reservoir. The channel was constructed around a length of aluminium channel, inverted and to which were bolted lengths of 10 mm thick acrylic sheet to form the sidewalls of the channel. A schematic representation of the apparatus is shown in figure 3.

A centrifugal pump, driven by a speed-controlled motor, was used to return the oil through a heat-exchange unit to the upstream reservoir. The purpose of the heat-exchange unit was to maintain the oil at a stable working temperature, usually within ±0.02 K, during the course of an experiment, and the controlled pump speed (nominally 1 part in 10^4) ensured that the flow rate was held nearly constant during a given experiment.

A mercury bulb thermometer was located in the upstream reservoir, as indicated in figure 3. The oil temperature, which was noted at frequent intervals, was measured

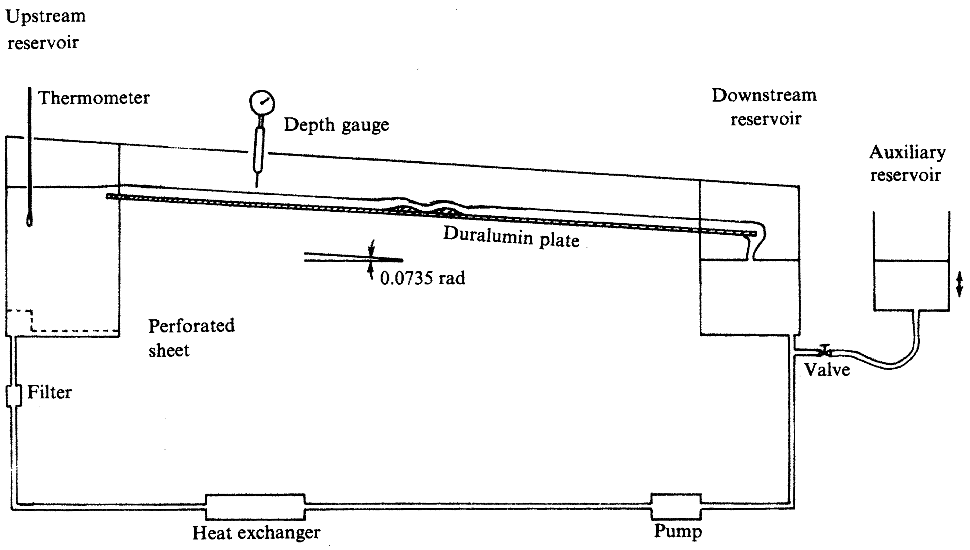

Figure 3. Schematic layout of the apparatus.

to within an uncertainty of approximately ±0.01 K. The temperature of the laboratory was maintained at (21±0.5) °C and the oil temperature was usually stabilized at about 21 °C, however, for each individual experiment, the recorded temperature was used in order to specify accurately the viscosity of the oil.

The main unit rested on feet located under each of the reservoirs. Adjustment screws in the feet were carefully set to ensure that the bed of the channel was nearly horizontal in a direction normal to the main axis of the channel (i.e. in a direction normal to the sidewalls). The auxiliary reservoir was used to maintain a constant depth in the downstream reservoir when the flow rate was changed.

(*b*) *The channel bed*

A relatively uniform channel bed was obtained by glueing sections of duralumin plate onto the aforementioned length of aluminium channel. These sections were of uniform thickness except for one which was built up with two approximately sinusoidal ridges that spanned the width of the channel, and were located as shown in figure 3. The ridges were made from an epoxy resin, of the kind used for building up car bodies, bonded firmly onto one of the duralumin sheets. Since it was important that the ridges be independent of the cross-channel coordinate a staircase profile of the desired shape was milled into the resin and the staircase was smoothed off with a new coating of epoxy and then polished. Finally the plate was machined to width to fit snugly into the channel. In this way a nice smooth profile was obtained which, most importantly, was uniform across the channel to a very good accuracy. The gaps between the sheets of duralumin used to form the false bed of the channel were also filled with epoxy and rubbed smooth.

With the channel bed properly in place, the channel was located firmly on its attachments and the desired slope for the channel bed was fixed. The bed was brought to the horizontal in the cross-channel direction near its upper and lower ends by adjustments of the heights of the feet on which the channel rested. Measurements were then made, relative to the free surface of a stationary liquid, at a number of locations along the channel to check that the bed was truly horizontal across the channel. The worst cross-channel twist was approximately 1 part in 1000, which was less than 1 % of the down-channel slope.

As indicated in figure 3, the channel bed consisted of an initial plane section of approximately 460 mm, followed by the two approximately sinusoidal ridges which stretched a further 200 mm downstream, and finished with another plane stretch extending a further 650 mm downstream. The plates used for the upstream and downstream sections of the bed were nearly planar, the upper surface of each deviating from a plane by less than 0.02 mm. The joints between these plates were, as described above, filled with epoxy and polished smooth; there were, however, small disparities in height across the joints of approximately 0.05 mm. One joint was located approximately 115 mm upstream of the crest of the first ridge, the second joint was approximately 85 mm downstream from the crest of the second ridge, and the third joint was a further 300 mm downstream. These small jumps seemed not to be important to the general structure of the flow field.

The profile of the channel bed, measured along the centreline of the channel, is given in figure 4*a*. For this figure distances, $\tilde{x}$, along the channel have been scaled by the distance D ($= 100.0$ mm) between the two crests of the ridges, and distances, $\tilde{y}$, normal to the flat sections of the channel have been scaled by the maximum height, b_0 ($= 10.0$ mm) of the ridges. The origin for the coordinate system shown in figure 4*a* is a preassigned point on the bed of the channel at a location near the inlet of the channel, and the coordinate direction along the channel is that defined by a line chosen to give the best mean representation of the measurements along the centreline in the flat portions of the channel. (The way this plane was chosen is described below.) Denote the coordinates along and normal to the channel respectively by $(\bar{x}, \bar{y}) := (\tilde{x}/D, \tilde{y}/b_0)$, and let the height of the channel bed above the line $\bar{y} = 0$ be given by $b(\bar{x})$. The measured values are indicated by the small ellipses, and the curve that interpolates these data points is a least-squares spline approximation. The locations of the knots used for the (cubic) spline approximation are indicated in figure 4*b* which also shows the difference between the interpolating function and the measured bed profile. Thus, it is seen that the error in using the indicated interpolation to represent the bed profile is no more than about 0.8 % (or about 0.08 mm) of the height of the ridges. We have used this interpolating function to define the lower boundary of the computational domain. An indication of the smoothness of the spline approximation is given in figure 4*c* and *d* where the first and second derivatives of the spline are shown. These graphs illustrate how well the approximations indicated in figure 4*a* and *b* were achieved without having to introduce unduly many oscillatory components to the spline. Such components would, for example, arise if too many knots had been used to make the spline conform closely to the original data.

As is evident from figure 4*a*, the channel along the centreline was, indeed, nearly flat upstream and downstream of the ridges. Thus we have used the data lying in the intervals $[-0.70, 3.10]$ and $[5.40, 7.00]$ of the downstream coordinate $\bar{x}$ to define a plane which can be used as a reference surface for the channel bed. (This plane was taken to be horizontal in the cross-channel direction.) A least-squares linear regression was fitted to the data in these intervals and was found to give a very good representation of the flat portions of the bed, except for the region near the very downstream end of the channel where, it transpires, the final duralumin plate had been installed at a small angle relative to the rest of the bed. The maximum deviation

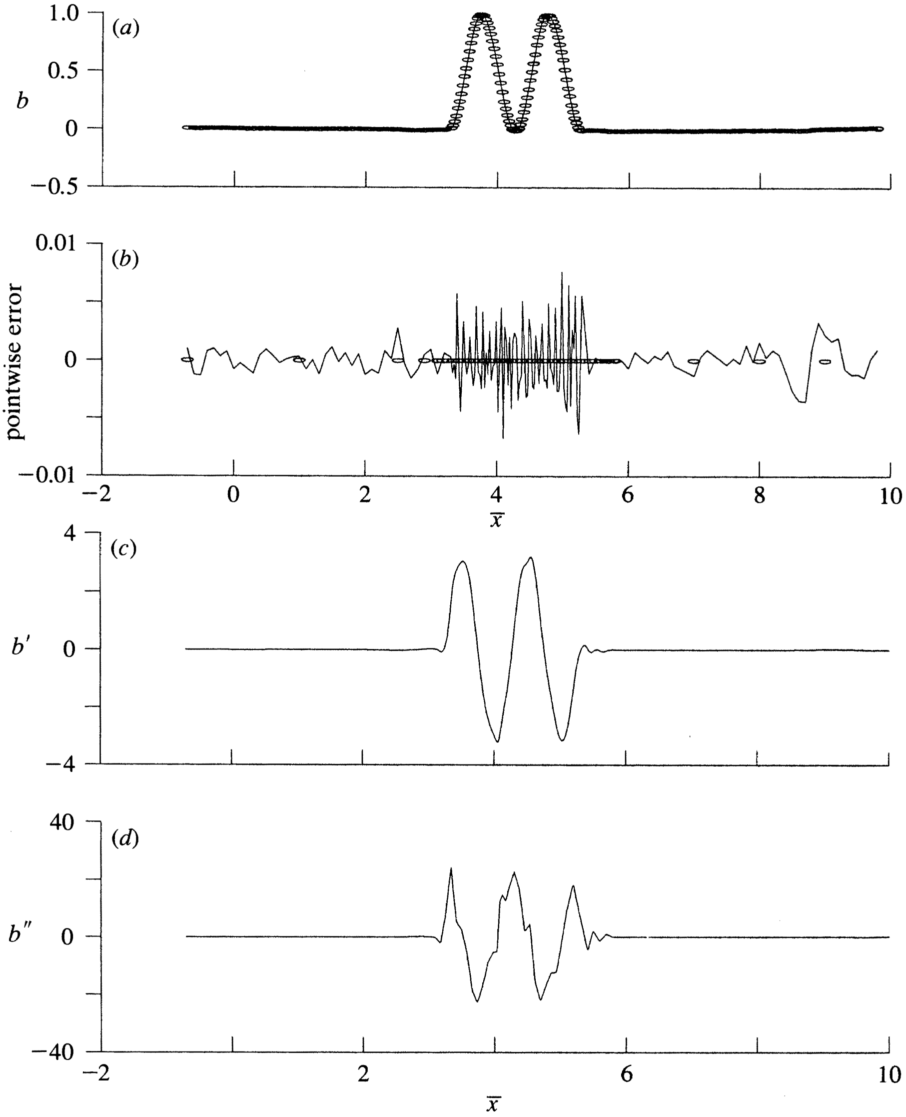

Figure 4. Measured profile of the channel bed. (*a*) ○, The measured profile; the approximating curve is a spline interpolation of the data; (*b*) the difference between the spline interpolation in (*a*) and the measurements. ○, The location of the knots for the spline; (*c*) the first derivative of the interpolating spline; (*d*) the second derivative of the interpolating spline.

of the supposedly flat portion of the channel from the reference plane thus chosen was 0.25 mm which, as seen in figure 5, was at the very downstream end of the channel. Shown in this figure are the reference plane for the channel bed, the measurements of the centreline bed height above the reference plane, and the spline representation of the data. Note that, in figure 5, heights above the channel bed have been considerably magnified, and distances along the channel have been considerably foreshortened. The slight misalignment of the very downstream part of the channel bed does not appear to have led to any difficulties in interpreting the experimental results.

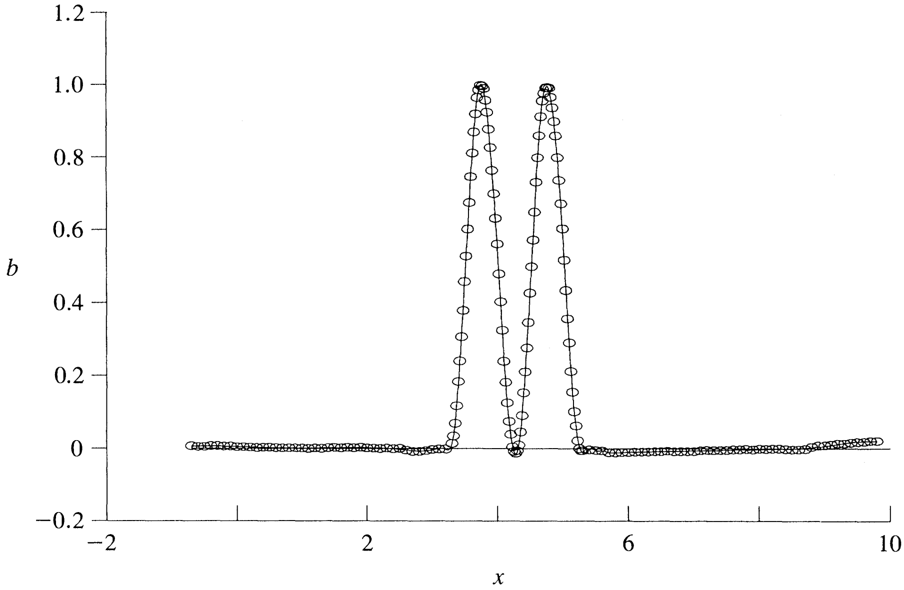

Figure 5. The data of figure 4*a* redrawn together with the plane used to represent the flat portions of the channel.

The reference plane, as defined above, gives the mean slope of the flat portion of the channel to the horizontal. This angle was determined to be 0.0735 rad, as indicated in §3*a*.

(*c*) *The working liquid*

The liquid used in these measurements was a commercial vegetable oil of the kind used in the catering industry. This oil was a blended mixture of a variety of vegetable oils, but is believed to have been derived predominantly from oilseed rape. One minor inconvenience of this oil was that its mechanical properties, in particular its shear viscosity, showed small changes with use. This kind of oil has been used in our laboratory for several years and it has been found that, when in regular use, its shear viscosity changes by roughly 0.04% per day. Thus, the viscosity of the oil was monitored on a regular basis throughout the course of the experiment. It is believed (see Pritchard 1986) that any non-newtonian properties of this material were of negligible importance in the present experiments, and that the shear viscosity was independent of the shear rate over the range of operating conditions used in the experiments.

Near the usual operating temperatures for the present experiments the (shear) viscosity of the oil was found to change by approximately 3.7% per degree kelvin, the viscosity decreasing with increasing temperature. Therefore, to be able to specify the viscosity of the oil in a given experiment, it was important not only to monitor carefully the physical effects of ageing, but also to determine accurately the operating temperature for each experiment.

Relative changes in the viscosity of the oil were monitored by measuring the time for a given quantity of fluid to discharge through a capillary viscometer. This time was determined to a reproducible accuracy of better than 0.1% and so relative changes of the viscosity could be tracked very closely. The absolute viscosity was determined by comparison of the viscosity of the oil with that of distilled water, the value of which was taken from international standards. The kinematical viscosity of the oil was approximately 0.8 stokes (or $80\times10^{-6}\ \mathrm{m^2\,s^{-1}}$), which is roughly 80 times the viscosity of water at the same temperature. The actual viscosity for a given experiment was known to within 1%.

The surface tension of the oil was determined in two ways. The force exerted on a thin plate, whose edge had been brought down to touch the surface of the oil, was measured and this quantity was used to estimate the surface tension. (The contact angle of the oil with the plate surface was observed to be very small and so, for these estimates a contact angle of zero was assumed.) The second method consisted of determining the force acting on a circular ring of wire drawn out through the liquid surface. Initially the experimental procedures were established by determining the surface tension of highly purified water.

From these two kinds of measurements the surface tension of the oil, determined at a temperature of 21 °C, was estimated to be $33.0\pm1.0\ \mathrm{dyn\,cm^{-1}}$.

The density of the oil was measured by using a relative density bottle and was estimated to be $0.922\ \mathrm{g\,cm^{-3}}$ at a temperature of 21 °C.

(*d*) *Depth measurements*

All measurements of the free surface location were made by carefully lowering a pointer until it just broke the free surface of the liquid. The pointer gauge was fixed into a piece of brass rod on the upper end of which rested the leg of a dial gauge. Detection of the moment the needle broke the free surface was easily recognizable because of surface tension immediately pulling the liquid up the shaft of the needle; however, because the working liquid was, in this case, a very poor electrical conductor, care had to be taken that no charge built up on the needle as this could also cause the liquid surface to dimple before the needle point had actually reached the surface. With reasonable care it was possible to reproduce the depth measurements to within ±0.01 mm. The maps of the channel bed (cf. §3*b*) were also made by lowering a needle until it just met the surface.

(*e*) *Specification of the upstream and downstream boundary data*

The asymptotic velocity profiles upstream and downstream have been determined from measurements of the depth of liquid flowing down the uniform sections of the channel.

Consider a viscous fluid flowing, under the action of gravity, down a plane surface inclined at an angle α to the horizontal. Suppose that the thickness of the sheet of liquid on the plane surface is H and that $\tilde{y}$ measures the normal distance above the plane. Then the Poiseuille velocity distribution $\tilde{u}(\tilde{y})$ for steady flow down the plane is

$$\tilde{u}=\frac{gH^2\sin\alpha}{2\nu}\left[2\left(\frac{\tilde{y}}{H}\right)-\left(\frac{\tilde{y}}{H}\right)^2\right], \tag{3.1}$$

where ν is the kinematical viscosity of the fluid and g is the gravity constant. Corresponding to this flow, the volume flux, Q, per unit width is

$$Q=(gH^3\sin\alpha)/3\nu, \tag{3.2}$$

and the velocity at the free surface is equal to $(\frac{3}{2}Q/H)$. Based on the analysis of Abergel & Bona (1992), we know that the flow fields over the uniform parts of the channel are close to their asymptotic states far away from the perturbed part of the channel bed, so the depth in these regions can provide a convenient means of specifying the basic flow parameters for the experiment, in particular the inflow and outflow boundary conditions for the numerical solutions. That the above distribution (3.1) did indeed give a good description of the flow in the channel was checked by direct measurements of the surface speed which agreed, over the complete range of operating conditions, to within 1.5% of that predicted from (3.1) by using the empirically determined values of H, α and ν. Also, above the uniform sections of the channel, the sheets of liquid were found to be very nearly of uniform thickness, at least in the regions away from the ridges, indicating that the film had achieved an equilibrium between the gravitational acceleration and the viscous stresses, in agreement with the theoretical discussion given in §§1 and 2*a*.

As indicated above, the depth measurements were accurate to within approximately ±0.01 mm. Thus, for a depth of 1 mm, corresponding roughly to the smallest flow rate used here, the accuracy of the determination of H corresponds to a 3% error in the specification of Q (cf. (3.2)). At the larger flow rates the upstream depth was of the order of 10 mm, so, under these conditions, the relative error in determining Q from depth measurements was quite small.

(*f*) *The experiment*

The procedure adopted in these experiments was as follows. The desired flow rate was established and the oil was allowed to equilibrate to the control temperature. Measurements of the free surface height were then made along the centreline of the channel using the pointer gauge described above in §3*d*. The position along the channel was established by reference to an engraved steel rule glued to the side wall of the channel. Thus, by aligning the pointer gauge with one of the graduations on the rule, the down-channel location, $\tilde{x}$, was known to within approximately ±0.1 mm. Measurements were also made at potentially critical locations of variations of the free-surface height across the channel. Three-dimensional structure across the channel emanated most noticeably from the side walls of the channel where the fluid passed over the ridges, and became quite pronounced at the largest flow rate used in the experiments. Depth measurements at a specific location were made repeatedly throughout the experiment to ensure that the flow rate remained nearly constant. The temperature of the fluid was also carefully monitored throughout the experiment to ensure that it was controlled to within ±0.2 K.

Care was taken throughout the experiment to look for possible unsteadiness of the flow. One reason for this precaution was the potentiality of a long-wave instability of the free surface when the Reynolds number exceeds a critical value $R_{\mathrm{c}} = \frac{5}{6}\cot\alpha$ (Yih 1969, p. 502). In the present experiments $R_{\mathrm{c}} = 11.3$, but there was no indication from the observations that this potential source of instability was significantly important here, even at Reynolds numbers well above the critical value. However, at the very largest Reynolds numbers used, some unsteadiness was observed in the zone between the two ridges. More detailed discussion of this point is given below in the description of the experimental results.

One curious feature of the flow, which is not understood by us, was the development of small surface patches mainly originating near the upstream end of the channel. These patches, which grew to a diameter of about 15 mm, were reminiscent of the spreading of a small amount of a contaminant on the surface of a liquid. Degassing the oil did not have any effect on the appearance of the patches.

4. Numerical experiments

Some experiments were carried out to check the performance of the numerical code in predicting the exact solution of certain problems. Such tests are usually very helpful on several counts. In particular, they indicate whether or not the implementation has the expected convergence properties as the mesh is refined, and they can also give a good indication of the mesh refinements needed to achieve a desired accuracy. Another benefit of these kinds of tests is that appropriate choices for parameters associated with the convergence of iterative parts of the scheme (cf. §2*e*(ii) in the present context) can be established. We have made numerical experiments of this kind on two particular problems. The first, made in a fixed domain, provides a test of the basic Navier–Stokes solver. The second problem was used to test the free-surface aspects of the solution procedure.

(*a*) *Convergence studies*

(i) *Jeffrey–Hamel flows*

Convergence studies in a fixed domain have been made using the well-known Jeffrey–Hamel solution in two dimensions for steady flow into a converging duct (Landau & Lifschitz 1959, p. 81). This flow provides a similarity solution to the Navier–Stokes equation in which the velocity field, in cylindrical polar coordinates (r, θ), is assumed to be of the form $(6\nu f(\theta)/r, 0)$ suggested by the continuity equation, where f is a function only of θ, and ν is the kinematical viscosity of the fluid. We suppose that the flow is confined to the wedge $0 < \theta < \alpha$, with α less than $\frac{1}{2}\pi$. The assumption of such a flow structure leads to a nonlinear ordinary differential equation for f. The solution of this ordinary differential equation then permits a definition for the Reynolds number, R, which we write as

$$R := 6\int_0^\alpha f(\theta)\,\mathrm{d}\theta. \tag{4.1}$$

In the computational tests to be described we restrict the flow domain to a bounded subset of the wedge, excluding a neighbourhood of the origin. For the most part we have used a flow domain bounded on the left by a plane passing through the point $(r_1, 0)$ orthogonal to the wall of the wedge at that point, and similarly on the right by a plane passing through the point $(r_2, 0)$, examples of which are given in figure 6. Dirichlet data for the velocity fields on these two planes were determined from the exact solution which, together with the no-slip boundary condition on the walls of the wedge, provide a well-posed problem for the Navier–Stokes equation, for which problem a solution is the self-same Jeffrey–Hamel flow. As indicated above the exact solution is given only in terms of an ordinary differential equation and therefore has to be found numerically. This was done by means of a (second-order) finite-difference scheme, and utilizing a Newton iteration to resolve the nonlinear problem. To define the pressure field uniquely, we have determined the arbitrary constant associated with the pressure solution such that the pressure has a mean value of zero when integrated over the flow domain, in keeping with the definition (2.12) for the pressure space Π.

Convergence studies have been made for both the implementations QLT and bQLQ defined in §2*d* (and see §2*e*). A sequence of triangulations, geometrically similar to the one shown in figure 6*a*, was used for the convergence study of the QLT method.

MATHEMATICAL, PHYSICAL & ENGINEERING SCIENCES
THE ROYAL SOCIETY A
PHILOSOPHICAL TRANSACTIONS OF

Figure 6

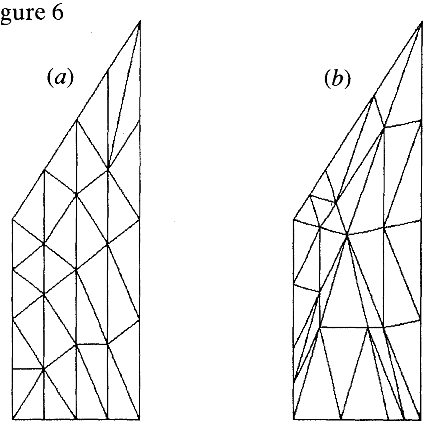

Figure 7

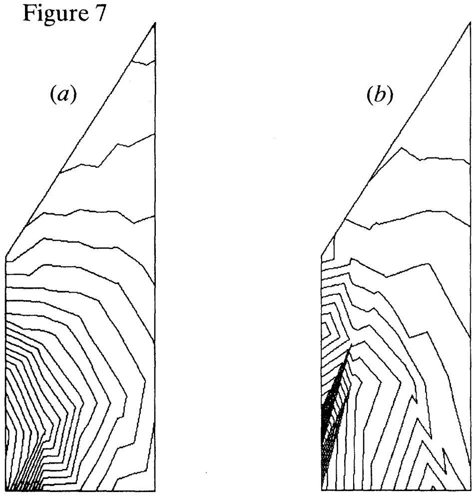

Figure 6. Examples of the triangulations used for the convergence studies based on Jeffrey–Hamel flow in a wedge. (*a*) The mesh used for the main study; (*b*) a distorted mesh. The domain is bounded on the left by planes through the points (1, 0) and (2, 0) respectively; the wedge has angle $\alpha = 1$.

Figure 7. The pressure fields at $R = 0.082$ generated by the QLT solutions when using the respective meshes (*a*) and (*b*) shown in figure 6. (*a*) The equally spaced pressure contours took values between 10.35 and 10.76; (*b*) the pressure contours shown were those obtained after 15 nonlinear iterations and took values between -1.7413×10^5 and -1.7412×10^5.

The quadrilateralizations used to study the bQLQ implementation were based on the vertices of the triangulation shown in figure 6*a*. For the triangulations, exact similarity was achieved by successive refinement of a coarse mesh, in which new triangle vertices were introduced at the bisectors of each triangle edge. The parameter h used to characterize the mesh sizes was chosen to be

$$h := \left(\max_{\tau\in\mathscr{D}_h}\{|\tau|\}/|\Omega|\right)^{\frac{1}{2}}, \tag{4.2}$$

where $|\tau|$ denotes the area of a triangle (or quadrilateral) and $|\Omega|$ denotes the area of the flow domain. The triangulation shown in figure 6*b* was designed to have some poorly shaped triangles to see if such a triangulation would affect the convergence properties of the method. In fact, we were unable to get the scheme to converge to a solution on the mesh shown in figure 6*b*, and it is suspected that the difficulties arose from the approximation of the pressure field, an example of which, after 15 Newton iterations had been made, is shown in figure 7. Here are given equally spaced contours of the pressure fields obtained at a Reynolds number of 0.082, as used in the convergence studies described below, on each of the meshes shown in figure 6. The contours for the pressure field obtained on the more regular mesh (see figure 7*a*) are a reasonably good approximation to the exact solution, whereas the contours shown in figure 7*b* do not provide a good approximation. This experiment suggests that some care should be taken not to let the meshes become too distorted as the free surface iterations proceed.

The convergence studies were carried out to see how nearly the implementations recovered the estimate (2.58) and, to this end, the 'error constants'

$$E_r(\mathscr{I}_h\boldsymbol{u}-\boldsymbol{u}_h)/h^3E_r(\mathscr{I}_h\boldsymbol{u}) \quad \text{and} \quad E_r(\mathscr{I}_h p-p_h)/h^2E_r(\mathscr{I}_h p),$$

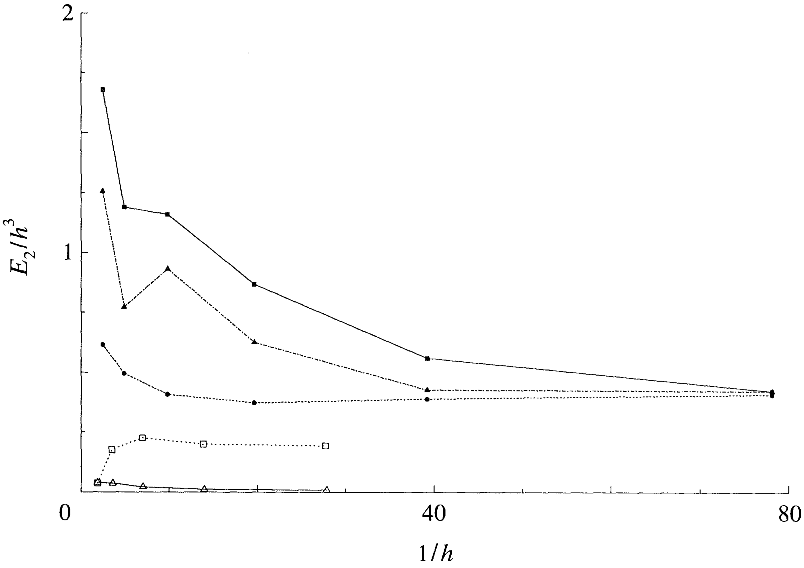

Figure 8. Convergence properties of the velocity fields for numerical solutions of Jeffrey–Hamel flow. ■, ——, $R = 0.082$, QLT method; ▲, –·–, $R = 18.1$, QLT method; ●, – – –, $R = 0.082$, highly symmetrical mesh, QLT method; □, ----, $R = 0.082$, bQLQ method; △, ——, $R = 0.082$, highly symmetrical mesh, bQLQ method.

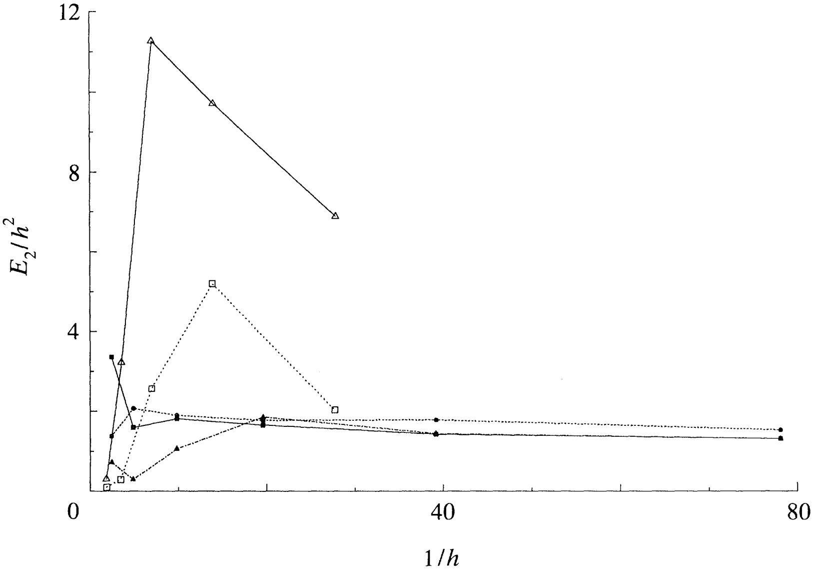

Figure 9. Convergence properties of the pressure fields for numerical solutions of Jeffrey–Hamel flow. ■, ——, $R = 0.082$, QLT method; ▲, –·–, $R = 18.1$, QLT method; ●, – – –, $R = 0.082$, highly symmetrical mesh, QLT method; □, ----, $R = 0.082$, bQLQ method; △, ——, $R = 0.082$, highly symmetrical mesh, bQLQ method.

for $r = 1, 2$ and ∞, have been determined on a sequence of meshes. The results for the convergence of the velocity fields, for $r = 2$, are shown in figure 8, and for the pressure fields in figure 9. Here the errors have been plotted as a function of h^{-1} to display clearly the structure on the finer meshes, and the symbol E_2 denotes the normalized error referred to above. It is seen from figure 8 that the velocity fields converged at a rate proportional to h^3, as expected theoretically. For the QLT method the constant of proportionality was just less than 0.5, for each of the triangulations tested here and for the calculations at both the smaller and the larger Reynolds numbers. The highly symmetrical mesh referred to in figure 8 was a symmetrical mesh based on a domain that approximated an annular sector of a circle, whereas the basic mesh was of the kind depicted in figure 6*a*. It is seen for the bQLQ method that the constant of proportionality associated with the convergence of the velocity field was somewhat smaller than that for the QLT method, especially when using the symmetrical domain and regular quadrilateralization. (Note that the convergence studies for the bQLQ method were not carried out on the finest mesh used for the QLT studies because of difficulties in obtaining a converged solution.)

The convergence plots for the pressure fields, shown in figure 9, indicate that the theoretically expected convergence properties for the QLT method were nearly realized on the meshes used in the study. By contrast, the results shown for the bQLQ method do not show the normalized pressure error to be proportional to h^2, for small h, as expected theoretically. Further details of the pressure field will be described below when discussing the results relating to figure 12.

The above convergence studies should provide a rough idea of the accuracy achievable on a given mesh in the numerical experiments associated with the experimental situation.

(ii) *Static meniscus*

To provide some kind of check on the free-surface capability of the numerical procedures, convergence studies have been carried out by computing the shape of the meniscus of the free surface of a liquid near a plane vertical wall. Suppose that the rigid wall lies along the line $x = 0$ and that the liquid domain is of infinite extent in the direction of positive x. Let the free surface be denoted by $\zeta(x)$, and we suppose that the origin for the vertical coordinate y is chosen to correspond to the asymptotic height of the free surface at large distances from the wall. Since the liquid is assumed to be at rest, the momentum equation takes a particularly simple form, yielding the familiar hydrostatic pressure field. The absence of fluid motion means that the stress field is everywhere isotropic and equal to the pressure. Thus (2.7) can readily be evaluated, but we must first specify the length H used to scale the equations. The natural length scale presented by the present problem is $(T/\rho g)^{\frac{1}{2}}$, in terms of which the solution to (2.7) is given by (cf. Landau & Lifschitz 1956, p. 235)

$$\zeta(x) = 2\{\cosh[x + \cosh^{-1}(\surd(2/(1-\sin\alpha)))]\}^{-1}, \tag{4.3}$$

and the maximum elevation of the free surface, at $x = 0$ is $\zeta(0) = \surd(2(1-\sin\alpha))$.

For the numerical experiments to be described, the contact angle α was chosen to be 1 rad and the flow domain was chosen to extend to a depth of $-5.3\zeta(0)$ and to have a width of $31.6\zeta(0)$. An initial triangulation of the domain was derived from a graded quadrilateralization of the region enclosed by the exact representation of the free surface and the boundaries just indicated. The grading was chosen such that the ratios w_i/w_{i+1} and d_i/d_{i+1} of the widths w_i, w_{i+1} and the depths d_i, d_{i+1} of adjacent quadrilaterals were constant for a given quadrilateralization. Thus, the smallest triangle in a tesselation was located at the corner between the meniscus and the side wall of the domain. The left- and right-hand sides of each quadrilateral were vertical lines, which formed the so-called spines (cf. §2*e*), and along which nodal points were

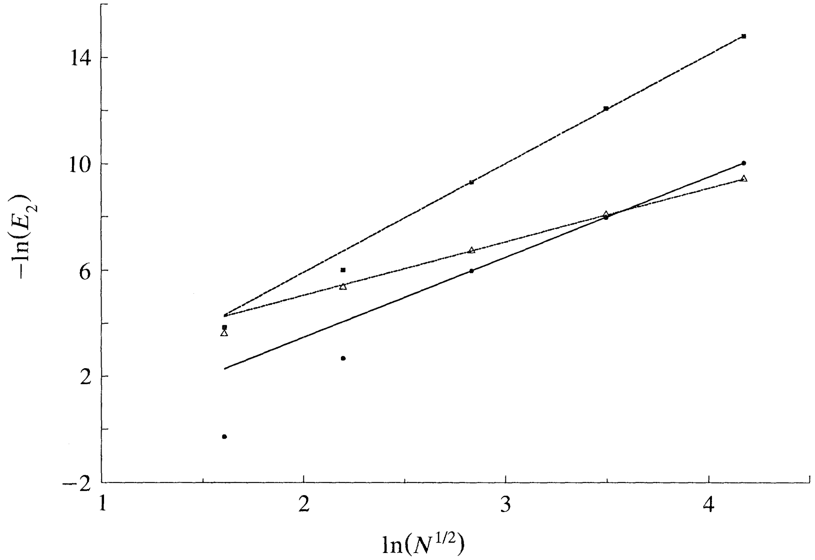

Figure 10. Convergence study for the static meniscus problem using the QLT method. Here N denotes the number of nodal points in the triangulation and E_2 measures the difference between the computed and the exact solution. ——■——, Velocity field; ——●——, free surface profile; –·–△–·–, pressure field.

relaxed during the iterative procedure to determine the free surface. The horizontal velocity u was set to zero along the bottom and along the two side boundaries of the domain. The vertical velocity v was also assigned in the same way, except for the two nodal points at which the free surface met the vertical boundaries. Setting $v = 0$ at these points resulted in a method that did not converge as the mesh was refined.

The results of our numerical experiments on the meniscus problem using the QLT method are summarized in figure 10. Because of the grading used in constructing the triangulation and because of the modification to the mesh during the solution procedure, it was decided to characterize the mesh refinement by the number, N, of nodes associated with the triangulation. Thus, in figure 10 we have plotted, on logarithmic scales, the error E_2 between the free surface height, the velocity field and the pressure field, and computed counterparts of the same quantities. (Note that, in the case of the velocity field, which is identically zero for the exact solution, the error E_2 has not been normalized and the absolute values of the error have been used.) The error has been plotted as a function of $N^{\frac{1}{2}}$, the inverse of which should characterize well the mesh size h. A least-squares regression to the errors calculated on the three smallest meshes was found and these lines are shown in the figure. The slopes of these regression lines were 4.09 for the velocity field, 3.02 for the surface height and 2.01 for the pressure field. The apparent superconvergence for the velocity field is probably a consequence of the fact that the solution to the flow problem (namely zero velocity everywhere) lies in the space spanned by the finite-element approximation.

We were unable to complete a satisfactory convergence study for the meniscus problem by using the BQLQ method. The computational time increased so dramatically as the meshes were refined that it became impractical to complete the study. We had also wanted to carry out convergence studies for the meniscus problem on narrower domains, so that attachment conditions of either surface height or non-zero slope would be required at both ends of the domain. However, there appears to be no

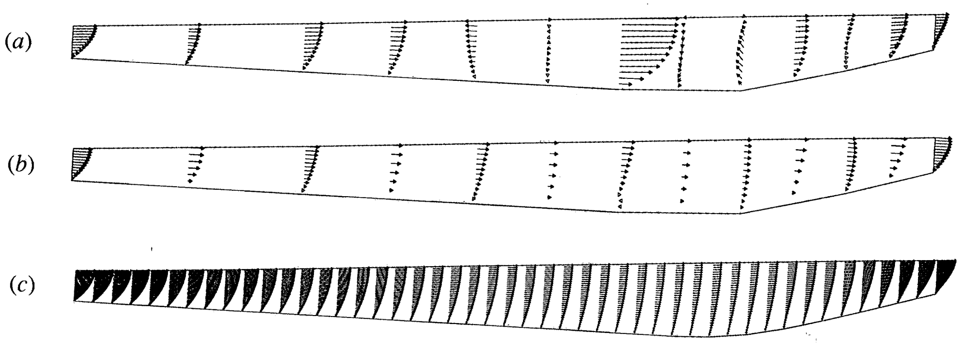

Figure 11. Examples of velocity fields computed for the experimental situation at $R = 0.369$. (a) and (b) are examples of results obtained on rather coarse meshes, and (c) was obtained on the mesh used for the main comparisons with the experimental results; (a) and (c) were obtained by using the QLT method, and (b) was obtained by using the bQLQ method. The velocities are given at the nodal points of the meshes, except that the velocity at the centroids of the quadrilaterals has been omitted in (b).

mechanism within the code to fix the pressure field at some given point of the flow domain and it is therefore not possible to relate the pressure field in the flow domain to that imposed by the region exterior to the flow.

(iii) *Flow on an inclined plane*

Before describing the main results it is instructive to try to estimate the accuracy of the computed solutions for the flow problem at hand. Since the physical experiments were accurate to within 1 or 2%, it is desirable that the numerical solutions have an accuracy considerably better than 1%, say to within the range 0.1–0.5%. To achieve such accuracy we see, from figure 8, that h should not exceed 0.1 for the velocity field to be accurate to within 0.1%, and the surface height should then be known to within about 1%. But, as indicated below, a mesh of this fineness, for the present flow calculation, provided an intolerably large calculation in terms of permissible memory and disk allocation, and also (to a lesser extent) in terms of the computational time required by the code. Compromises were therefore needed, though considerable care had to be taken to ensure that the meshes adopted allowed acceptable accuracy for the solutions. Some illustrations of results obtained on meshes that were too coarse are given in figure 11*a*, *b*, where velocity fields computed for the experimental situation at $R = 0.369$ are shown for the section of the channel lying between $x = 25.0$ and 35.7, just upstream of the first hump. The meshes used in these computations were based on a nearly rectangular grid of 61×6 points (123×13 velocity nodes), for the cases shown in figure 11*a*, *b*, and of 166×17 points (333×33 velocity nodes) for the case shown in figure 11*c*. There are evident problems associated with the coarser meshes, with the divergence condition not being at all well approximated, especially in the case of the QLT method. On the other hand, when using a finer mesh (see figure 11*c*), it is evident that the numerical solutions obtained from the QLT method respected the divergence constraint much more closely. Examples of the pressure fields obtained in the fine-mesh calculations (166×17 grid points) are given in figure 12. It is seen here that the continuous pressure element used by the QLT method provided a good representation of the linear gradient in the y-direction expected at very small Reynolds numbers, whereas the discontinuous element associated with the bQLQ method yielded significant jumps between

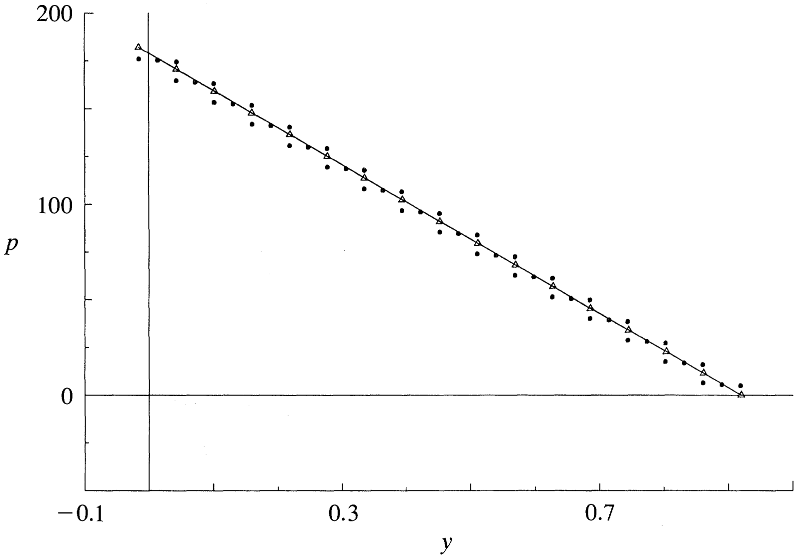

Figure 12. A comparison of the computed pressure fields p as a function of the height y above the reference plane. The pressures here were obtained at $x = 42.6$ at a Reynolds number of 0.369. —△—, The QLT method; ●, the bQLQ method.

quadrilaterals. On average the pressure field generated by the bQLQ method agreed closely with that obtained with the QLT method, but the reason for the large discontinuities in p between quadrilaterals is not clear. Similar results also obtained for slices of the pressure fields in the streamwise direction.

The computations made by using the fine mesh (cf. figure 9*c*) required 16 MB of core and a further 80 MB of disk space to store the factored stiffness matrix, and took the order of an hour to complete on a twin-processor Ardent Titan (P1) machine. We would have preferred to have made the main computations on a finer grid, but that was not routinely feasible as a halving of the mesh (i.e. a doubling of the number of nodes) required approximately 350 MB of disk space to effect the solution process. (The solution procedures used by the code when the linear system is too large to be held in the core memory are discussed by Hasbani & Engelman (1979).)

The spines (cf. §2*e*(ii)) used to constrain the movement of the grid points when determining the free surface height were chosen to be normal to the reference plane for the channel bed. The grid points were equally spaced in the y-direction along these spines but, in the x-direction, the spines were adjusted so that their horizontal spacing was closest in the regions where the magnitudes of the x-gradients of the flow field were largest. This meant that, with only 166 grid points at our disposal, the triangles or quadrilaterals in the upstream and downstream sections of the channel were rather elongated but, since the velocity and pressure fields in these regions are nearly quadratic and/or linear in their respective variables, it was hoped that the method would nevertheless provide good approximability in these regions. Thus, in the central zone of the channel, the spacing of the grid points was roughly 0.15 in the x-direction and 0.1 in the y-direction.

To help assess the accuracy of the main calculations two numerical experiments were carried out on the very fine mesh (667 × 67 velocity nodes) and the solutions were compared with those on the coarser mesh (333 × 33 velocity nodes) on which the main experiments were made. At $R = 0.369$ the difference in the surface heights ζ between the two computations was less than 0.5% in both the E_2 and E_∞ measures (cf. §2*d*, and see below in §4*b* for further details of how these quantities were determined) even though the velocity and pressure fields differed by approximately 1% in the E_2 measure and by 3–4% in the E_∞ measure. Paradoxically, at the larger Reynolds number of 7.59, the velocity and pressure fields differed by only 0.5% in the E_2 measure and by approximately 2.8% in the E_∞ measure; the surface heights in this case differed by approximately 0.4% in both the E_2 and E_∞ measures. The large differences in the E_∞ measures between the calculations on the coarser and fine meshes is somewhat disconcerting in view of the scale of the computations required to achieve such accuracy. On the other hand, the test does suggest that, in view of the anticipated convergence order of the method, the surface heights were found to an accuracy of better than 1% in the main computations.

(*b*) *The lubrication models*

It is instructive to examine how well the lubrication models presented in §2*c* are able to approximate the properties of the flows under consideration. To carry out this assessment we make comparisons both with the experimental data and with solutions obtained from our computed solutions to the Navier–Stokes equations. For the present discussion we assume that the numerical solutions provide a good approximation to the solution of the complete flow problem, anticipating the discussion in later sections of the paper.

The main comparisons to be reported are those of the predicted and the experimentally determined heights of the free surface above the plane $y = 0$, as defined in §3*b*, as a function of distance x $(:= \tilde{x}/b_0)$ along the plane. Let us denote the free-surface height, scaled by the height b_0 of the bumps, by the symbol ζ, suitably adorned to indicate whether the height has been determined experimentally, by computation or from the lubrication models. Thus let ζ_{C} denote solutions obtained by finite-element computation, let ζ_{LX} denote the heights given by the standard lubrication model (2.36) and let $\zeta_{\mathrm{L}k}$, $k = 0, 1, 2, 4, \infty$, be those predicted by the improved lubrication models (2.45). The experimental free-surface heights will be denoted by the symbol ζ_{E}.

Quantitative comparisons between the variously determined surface heights were made in the manner described in §2*d*. Suppose that experimental measurements were made at locations x_i, $i = 1, \ldots, N$, and let $\mathscr{I}_h\zeta$ be an interpolant of an approximant determined from one of the theoretical models. Then we can use the 'error' formula (2.56) with the identifications that $\Sigma_\tau = \{x_i \colon i = 1, \ldots, N\}$ and $\mathscr{D}_h$ is the collection of intervals

$$[x_1, \tfrac{1}{2}(x_1 + x_2)], [\tfrac{1}{2}(x_{i-1} + x_i), \tfrac{1}{2}(x_{i+1} + x_i)] \quad \text{for} \quad 2 \leqslant i \leqslant N-1, \text{ and } [\tfrac{1}{2}(x_{N-1} + x_N), x_N].$$

It is convenient to normalize all such error formulae so that the errors can be expressed as a percentage of the appropriate norm of the function under consideration. We have chosen to normalize the formulae by the quantity $E_r(\zeta - \zeta(0))$, where ζ denotes the empirical data, where applicable, or else a computed solution. Note that the upstream height, $\zeta(0)$, of the free surface has been subtracted from the surface heights, ζ, so that only the perturbations of the free surface from the uniform stream are considered when estimating the 'size' of the functions being approximated. In the ensuing discussion it will be assumed that all errors have been normalized in this way, and therefore are often referred to as percentage errors.

Table 1. *Quantitative comparisons between the free surface heights* ζ_{Lk}, $k = 0, 1, 2, 4$ *and* ∞, *predicted by the improved lubrication models with experimental observations* ζ_{E} *and with numerical solutions* ζ_{C} *to the full mathematical problem, as determined by the* QLT *method*

(R is the Reynolds number; S is the surface tension parameter; $\zeta^*(0)$ denotes the upstream free-surface height; N gives the number of experimental observations. The errors E_2 and E_∞ are defined in §2*d*, and the norms Z_2 and Z_∞ are $E_2(\zeta_{\mathrm{E}} - \zeta_{\mathrm{E}}(0))$ and $E_\infty(\zeta_{\mathrm{E}} - \zeta_{\mathrm{E}}(0))$ respectively.)

R	0.369	2.44	5.03	7.59	12.2
S	34.2	9.80	6.36	4.50	3.38
$\zeta^*(0)$	0.209	0.390	0.484	0.575	0.664
N	68	68	76	86	125
Z_2	13.1	12.9	13.3	13.7	14.7
$E_2(\mathscr{I}\zeta_{\mathrm{L0}} - \zeta_{\mathrm{E}})/Z_2$	0.010	0.015	0.045	0.081	0.148
$E_2(\mathscr{I}\zeta_{\mathrm{L1}} - \zeta_{\mathrm{E}})/Z_2$	0.012	0.016	0.022	0.038	0.067
$E_2(\mathscr{I}\zeta_{\mathrm{L4}} - \zeta_{\mathrm{E}})/Z_2$	0.012	0.016	0.020	0.033	none
$E_2(\mathscr{I}\zeta_{\mathrm{L}\infty} - \zeta_{\mathrm{E}})/Z_2$	0.012	0.016	0.021	0.033	none
$E_2(\mathscr{I}\zeta_{\mathrm{C}} - \mathscr{I}\zeta_{\mathrm{L0}})/Z_2$	0.0059	0.019	0.047	0.083	0.142
$E_2(\mathscr{I}\zeta_{\mathrm{C}} - \mathscr{I}\zeta_{\mathrm{L1}})/Z_2$	0.0048	0.0094	0.016	0.028	0.056
$E_2(\mathscr{I}\zeta_{\mathrm{C}} - \mathscr{I}\zeta_{\mathrm{L2}})/Z_2$	0.0048	0.0093	0.015	0.025	none
$E_2(\mathscr{I}\zeta_{\mathrm{C}} - \mathscr{I}\zeta_{\mathrm{L4}})/Z_2$	0.0048	0.0093	0.015	0.025	none
$E_2(\mathscr{I}\zeta_{\mathrm{C}} - \mathscr{I}\zeta_{\mathrm{L}\infty})/Z_2$	0.0048	0.0095	0.015	0.026	none
Z_∞	0.978	0.951	0.955	0.968	0.995
$E_\infty(\mathscr{I}\zeta_{\mathrm{L0}} - \zeta_{\mathrm{E}})/Z_\infty$	0.023	0.022	0.046	0.084	0.156
$E_\infty(\mathscr{I}\zeta_{\mathrm{L1}} - \zeta_{\mathrm{E}})/Z_\infty$	0.025	0.034	0.041	0.074	0.149
$E_\infty(\mathscr{I}\zeta_{\mathrm{L4}} - \zeta_{\mathrm{E}})/Z_\infty$	0.025	0.034	0.039	0.061	none
$E_\infty(\mathscr{I}\zeta_{\mathrm{L}\infty} - \zeta_{\mathrm{E}})/Z_\infty$	0.025	0.034	0.039	0.068	none

Numerical solutions to the standard lubrication model (2.36) were obtained by using a fourth-order Runge–Kutta method. (A check of the procedure was also made by using a backward Euler method on a very fine mesh, and the test indicated that the numerical approximations to (2.36) reported herein were accurate to within 0.1%.) The third-order models (2.45), incorporating surface tension effects, were solved by using a high-order package (COLNEW) for two-point boundary-value problems (cf. §2*c*) and again the mesh size was chosen to be fine enough to ensure an accuracy of better than 0.1% for the numerical solutions.

Before giving a detailed description of the comparison of the various lubrication models with the experimental results it is worthy of note that the lubrication model, L0 (equation (2.35)) incorporating the effects of surface tension and the model LX, not including the surface tension effects (equation (2.36)) yielded very nearly the same solutions. So, for example, under the conditions corresponding to a Reynolds number of 12.2 (for which $S = 3.38$), the solutions to (2.35) and (2.36) differed by less than 0.68% in the E_∞ measure and for a Reynolds number of 0.369 ($S = 34.2$) the E_∞ difference was less than 1.31%. In both cases the E_2 differences were less than 0.5%. By contrast, it was found (see below and in table 1 for details) that the inclusion of a term allowing for inertial effects had a significant influence on the solution. So, for example, at $R = 7.59$, the free surface height predicted by the L0 model differed from the experimental results by 8.1% (in the E_2 measure), whereas the predictions from the L1, L2, L4 or L∞ models differed by less than 4% from the experimental measurements. Thus, it is seen that the surface-tension forces played only a very minor role in the quantitative comparisons to be described; however, as explained in §2*c*, the inclusion of the third-order derivative in (2.45) significantly

PHILOSOPHICAL TRANSACTIONS OF THE ROYAL SOCIETY A MATHEMATICAL, PHYSICAL & ENGINEERING SCIENCES

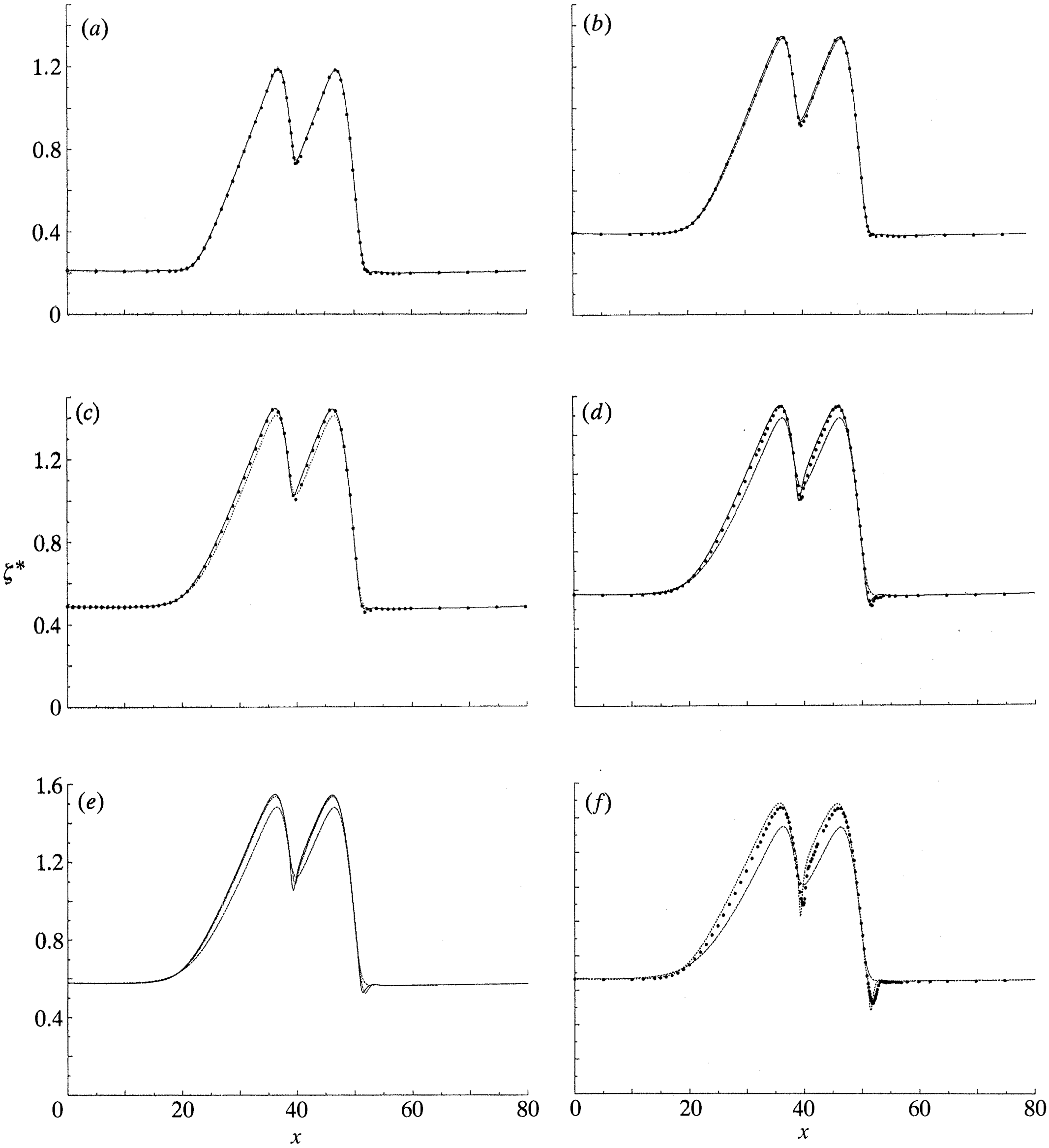

Figure 13. Comparison of the free-surface heights $\zeta^*(:= H\zeta/b_0)$ predicted by the lubrication models with experimental observations and with numerical solutions to the full mathematical problem. ●, Experimental values; ---, lubrication model L0 of (2.45); · · · · ·, lubrication model L1 of (2.45); ——, lubrication model L4 of (2.45); –·–, finite element solution. Lubrication models L0 and L4 compared with experimental observations: (*a*) $R = 0.369$; (*b*) $R = 2.44$; (*c*) $R = 5.03$; (*d*) $R = 7.59$. (*e*) Lubrication models L0 and L4 compared with finite element solution, $R = 7.59$; (*f*) L0 and L1 models compared with experiment, $R = 12.2$.

extended the range of Reynolds numbers for which numerical solutions were obtainable.

The efficacy of the models in describing the experimental observations is illustrated in figure 13 and quantitive comparisons are given in table 1. At the two smallest flow rates used in the experiments, for which $R = 0.369$ and 2.44, both the inertia-free

(L0) and the improved (L4) lubrication models closely represent the observations (see figure 13*a*, *b*). At $R = 0.369$ both lubrication models differed from the observations by only about 1% (in our E_2 measure) and by only about 2% at the very worst points. Moreover, both the models predicted surface profiles differing by only approximately $\frac{1}{2}$% from the profiles computed from the full equations. At $R = 2.44$, as seen in figure 13*b*, there were small differences between the two lubrication models but, even so, they both give a fairly good representation of the experimental observations. Note that, in figure 13 we have plotted the quantity $\zeta^*(:= H\zeta/b_0)$ rather than using the scaling based on the upstream height. Thus the height of the channel bed is the same in all sections of the figure (and see figure 14 below, where b is shown explicitly) and upstream and downstream depths are seen to be different at the different flow rates, corresponding to what is seen in the experiments. It should also be noted that the solution ζ to the basic lubrication model (2.36) is the same for all flow rates.

In contrast to the situation depicted in figure 13*a* and *b* there were considerable differences between the model L0 and the improved model L4 at a flow rate for which $R = 5.03$, as shown in figure 13*c* (and see table 1), and only the improved model gave a good representation of the observations. The results of quantitative comparisons are given in table 1 and it is seen there that the improved model differed from the experimental data by only 1.5% in the E_2 measure, whereas the standard model differed by 4.5%. (At the same flow rate, respective differences between the improved and standard models, in comparison with the finite-element solution were 1.5% and 4.7%.) At the flow rate for which $R = 7.59$ (cf. figure 13*d*) the differences between the two lubrication models became even more apparent. Again the improved model (L4) provided a reasonably good representation of the experimental results and, significantly, predicted the undulations, evident in the figure, in the lee of the downstream bump in the channel bed: the differences were only 3.3% in the E_2 measure and 6.5% at the worst. A comparison between the solutions of the lubrication models and the finite element solution to the full problem at $R = 7.59$ is shown in figure 13*e*, and we see that the improved lubrication model captures most of the structural details of the finite-element solution, whereas the model L0 badly misses many of the details at $R = 7.59$. Note that a phase-plane analysis shows that the L1–L∞ models always generate a small dip (when $R > 0$) in the lee of a bump, whereas the L0 and LX models do not.

At a Reynolds number slightly in excess of 7.59 the numerical schemes for the models L2 and L4 ceased to provide a solution and so, at a flow rate for which $R = 12.2$, the L0 and L1 predictions are given in figure 13*f*. It is seen here that the model L0 gives a very poor description of the observed surface heights, whereas the L1 model gives a tolerably good representation of the data, except for a considerable degree of overshoot at the troughs of ζ^*_{E}. This feature is reflected by the relatively small value of 6.7% for

$$E_2(\mathscr{I}\zeta_{\mathrm{L1}} - \zeta_E)/E_2(\zeta_E - \zeta(0)),$$

whereas the corresponding E_∞ value for the difference between the same two functions was nearly 15%. The model L1 failed to provide a solution at a flow rate corresponding to the experiment at $R = 16.2$. For the graphs shown in figure 13 we have mainly concentrated on the difference between the standard lubrication model L0, the improved lubrication model L4 and the experimental observations. In fact, for the range of experiments shown, the models L1 and L2 provided very nearly the same solutions as did the L4 model, which feature can be seen from the comparison

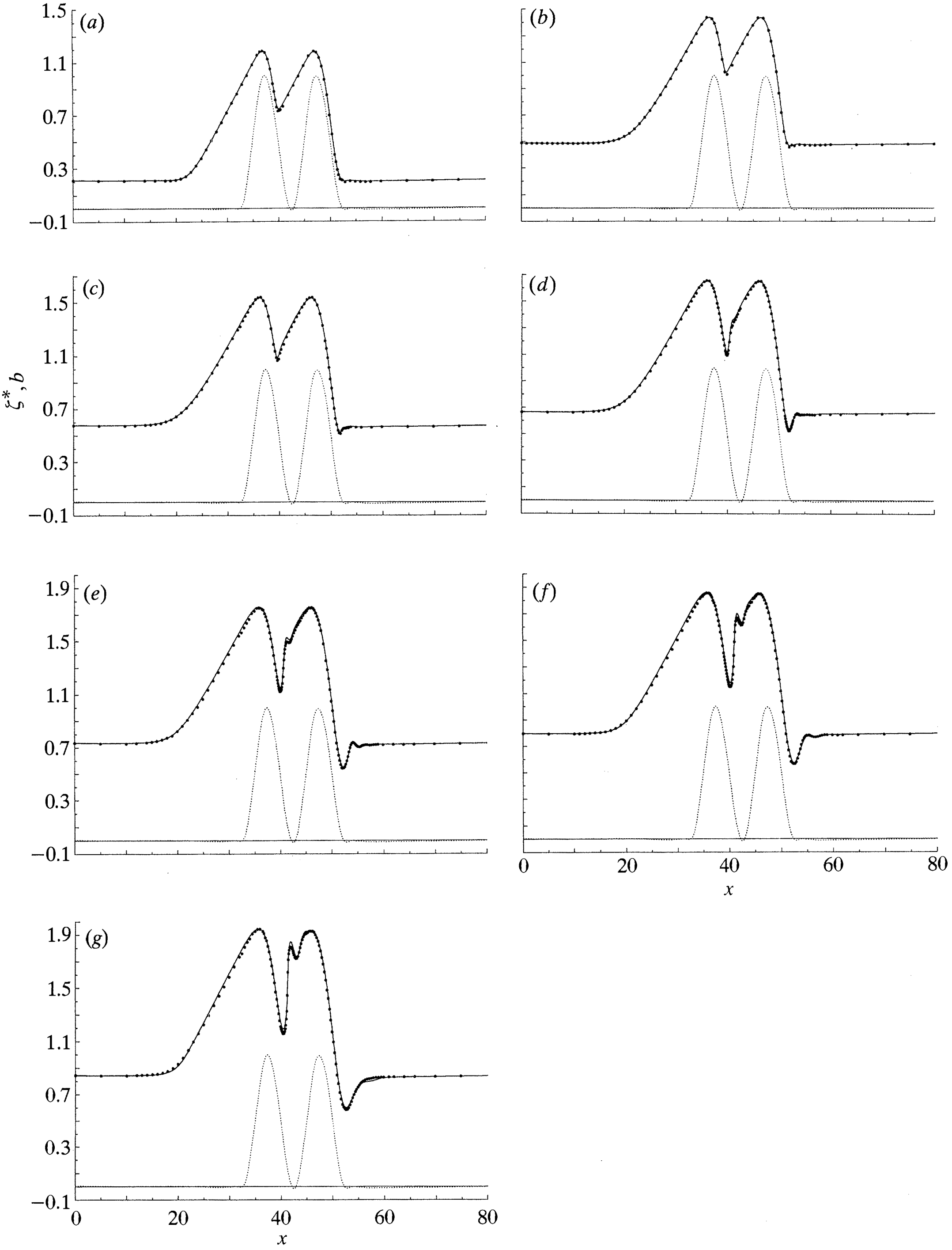

Figure 14. Comparison of the free surface heights ζ^* predicted by numerical computation (using the QLT method) and the experimental observations. ●, Experimental observation; ——, computed solution. The dotted line represents the bed, b, of the channel, and the solid base line represents the asymptotic reference plane. (*a*) $R = 0.369$; (*b*) $R = 5.03$; (*c*) $R = 7.59$; (*d*) $R = 12.2$; (*e*) $R = 16.2$; (*f*) $R = 20.5$; (*g*) $R = 25.5$.

Table 2. *Comparisons of the numerically determined, free-surface heights with the experimental observations* ζ_{E}

(Here $\zeta_{\mathrm{C}}, \zeta_{\mathrm{D}}$ refer respectively to solutions obtained by the QLT and bQLQ methods. R is the Reynolds number; S is the surface tension parameter; $\zeta^*(0)$ denotes the upstream free-surface height; N gives the number of experimental observations. The errors E_2 and E_∞ are defined in §2*d*, and the norms Z_2 and Z_∞ are $E_2(\zeta_{\mathrm{E}}-\zeta_{\mathrm{E}}(0))$ and $E_\infty(\zeta_{\mathrm{E}}-\zeta_{\mathrm{E}}(0))$ respectively.)

R	0.369	2.44	5.03	7.59	12.2	16.2	20.5	25.5	31.4	36.6
S	32.9	9.80	6.36	4.50	3.38	2.77	2.36	2.08	1.85	1.66
$\zeta^*(0)$	0.209	0.390	0.484	0.575	0.664	0.733	0.794	0.845	0.897	0.948
N	68	68	76	86	125	147	153	146	183	195
Z_2	13.1	12.9	13.3	13.7	14.7	15.7	16.9	18.2	19.4	20.2
$E_2(\mathscr{I}\zeta_{\mathrm{C}}-\zeta_{\mathrm{E}})/Z_2$	0.015	0.015	0.015	0.017	0.021	0.026	0.027	0.028	none	none
$E_2(\mathscr{I}\zeta_{\mathrm{D}}-\zeta_{\mathrm{E}})/Z_2$	0.013	0.014	0.015	0.017	0.022	0.028	0.029	0.028	none	none
Z_∞	0.978	0.951	0.955	0.968	0.995	1.02	1.06	1.10	1.16	1.18
$E_\infty(\mathscr{I}\zeta_{\mathrm{C}}-\zeta_{\mathrm{E}})/Z_\infty$	0.026	0.028	0.028	0.031	0.040	0.037	0.036	0.045	none	none
$E_\infty(\mathscr{I}\zeta_{\mathrm{D}}-\zeta_{\mathrm{E}})/Z_\infty$	0.024	0.027	0.028	0.031	0.041	0.038	0.040	0.045	none	none

shown in table 1 between the finite-element solution and that of the various lubrication models.

In terms of the present experiment, the above results suggest that the standard lubrication model provides a very good approximation to the full mathematical problem at Reynolds numbers less than about one, and that the improved models extended the range of applicability of the lubrication theories by an order of magnitude in the Reynolds number.

(*c*) *The finite-element approximations*

Detailed comparisons between the predictions for the free-surface height obtained using the QLT method and the experimentally determined heights are given in figure 14. Also shown in this figure, as a dotted line, is the bed b of the channel and the reference plane for the channel. The quantitative comparisons between the computed solutions, for both the QLT and the bQLQ methods, and the experimental results are given in table 2.

The agreement between the experimental observations and the numerical predictions is extremely close at the smaller Reynolds numbers, differing by less than 3% in the E_∞ measure for the cases $R = 0.369$, 2.44 and 5.03. For the flows at the Reynolds numbers of 7.59 (see figure 14*c*) and 12.2 (figure 14*d*) the numerical solutions captured the undulation in the lee of the second hump, but showed some small inaccuracies in the free surface structure in the region between the two humps. On the other hand, as shown in figure 14*e*,*f*, there is very good agreement between the numerical predictions and the experimental observations for the flows with $R = 16.2$ and 20.5, except for the region immediately upstream of the first hump. The downstream undulations in the free surface height near $x = 55$ were captured beautifully by the numerical solution in both cases.

At a flow rate corresponding to $R = 25.5$ considerable care was needed to obtain numerical solutions, and very small steps in the Reynolds-number continuation procedure were needed. The main obstacle appeared to be one of achieving convergence of the nonlinear solution procedure. In general terms, the numerical solution shown in figure 14*g* agrees reasonably well with the experimental observations, but there are significant differences near the local maxima and minima

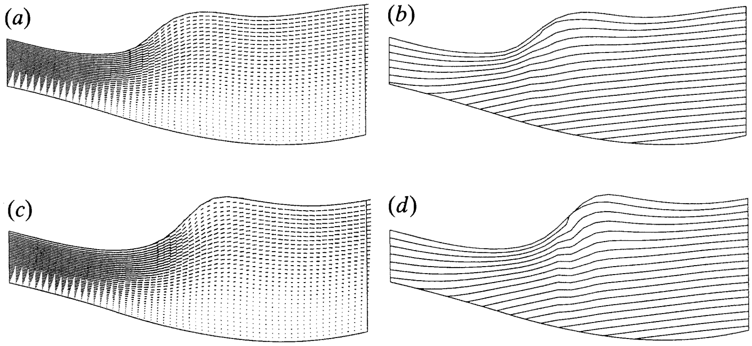

Figure 15. Computed velocity and pressure fields obtained, by using the QLT method, in the region between the two bumps where the surface slopes were greatest; (*a*) and (*c*) are velocity vectors at the nodal points of the mesh and (*b*) and (*d*) are pressure contours. (*a*), (*b*), $R = 20.5$; (*c*), (*d*), $R = 25.5$.

of ζ and, in particular, the numerical solution displays some structure in the region between $x = 55$ and 60 not evident in the experimental data. A quantitative comparison (see table 2) between the numerical solution and the experimental results shown in figure 14*g* indicates that the E_2 measure of the difference between the two functions is only 2.8% and that the E_∞ difference is 4.5%.

It was evident from the computations that the region where the surface slopes were largest was the most difficult to resolve numerically. Examples of the numerical solutions in this region are given in figure 15 for the experiments at $R = 20.5$ and 25.5. Here the velocity vectors at the nodal points for the computations are shown and contours for the pressure fields are also given, for that part of the flow domain with $x \in [39.0, 43.7]$. It is evident from these pictures that the free surface slopes were considerably larger and occurred at a slightly downstream location at the larger flow rate when compared with the flow at $R = 20.5$. But, in addition, it is seen, near the points of maximum surface slope, that the velocity vectors did not properly respect the kinematical condition at the free surface, and the pressure contours were not very smooth. We return to this issue below in §5.

A summary of the representation of the experimental observations by the various theoretical models is given in figure 16. We have given here the E_2 differences, to indicate an integrated difference between the models and the experimental results. The graph shows how, for the QLT finite-element computations the differences remained nearly constant over the range of Reynolds numbers (cf. table 2). The various lubrication models, by comparison, performed quite well up to $R = 2.44$, and the improved models gave a reasonable representation of the data up to $R = 7.59$, but these models either did not have any solution, or provided very poor approximations, at the larger Reynolds numbers.

(*d*) *Further experiments*

The measured surface profiles $\zeta^*(x)$ for flows at $R = 31.4$ and 36.6 are shown in figure 17. In general appearance the profiles shown here are not dissimilar from those shown in figure 14, though there are some evident differences upstream of the first hump and downstream from the second hump. One particularly noticeable aspect of these experiments at the larger flow rates was the very large surface slopes observed in the region between the two humps. Thus, for the experiments at $R = 20.5$ and 25.5

PHILOSOPHICAL TRANSACTIONS OF THE ROYAL SOCIETY A MATHEMATICAL, PHYSICAL & ENGINEERING SCIENCES

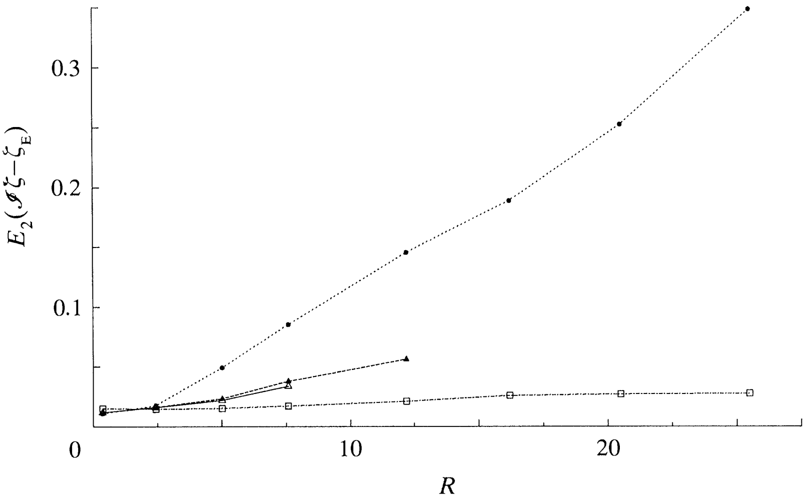

Figure 16. A summary of the E_2 differences between the predictions of various models and the experimental observations. ●, · · · · · ·, LX model; △, - - - -, L1 model; △——, L∞ model; □, –·–, QLT computation.

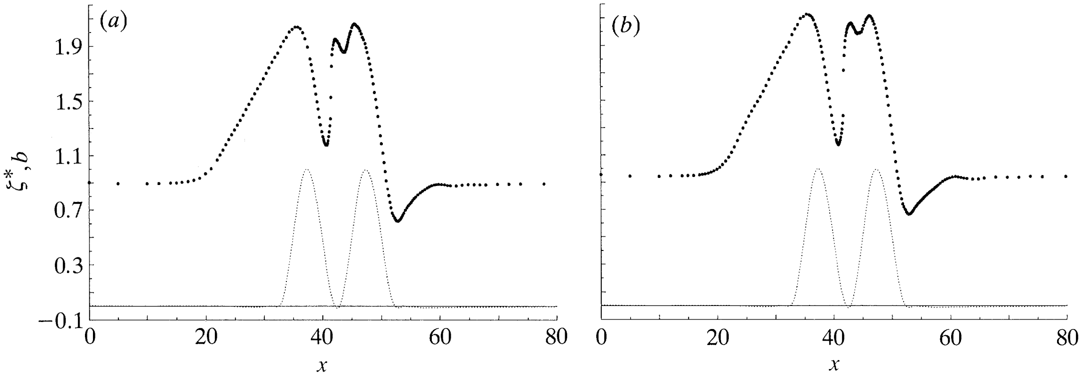

Figure 17. Free-surface heights measured at Reynolds numbers in excess of those for which numerical solutions were obtained. (*a*) $R = 31.4$; (*b*) $R = 36.6$.

the maximum observed surface slopes were approximately 45° and 60° respectively (cf. figure 15), whereas the maximum surface slopes for the respective experiments at $R = 31.4$ and 36.6 were 66° and 72°. (Note that the maximum slopes encountered at the smaller flow rates were of the same order as those of the slope of the bed. At $R = 0.369$, the maximum surface slope was approximately 17°, and at $R = 12.2$ it was approximately 19°.) Moreover, in the zone where the sharp jump in surface height took place, it was found, for the experiments at $R = 31.4$ and 36.6, that the free surface exhibited a small, but measurable, temporal variation in amplitude, of the order of ± 0.10 mm, compared with a total surface displacement of over 12 mm. Away from this sensitive region the flow was steady, at least to within the accuracy (0.01 mm) of our measurements. Any unsteadiness in the free surface heights at smaller flow rates (i.e. for $R \leqslant 25.5$) was insignificant enough not to have been especially noticed during the recording of the data.

Another potentially important aspect of the interpretation of the experimental data is the possibility of three-dimensional effects influencing the measurements at the centreline of the channel. A check was made in all the experiments to see if there were significant levels of non-uniformity across the channel. The most noticeable cross-channel variations were observed in the two experiments at the largest flow rates: the three-dimensional effects appeared to emanate from the flow on the leeward side of each hump, near the side walls of the channel, stretching out into the main flow at a relatively shallow angle of 10° or 15°. As indicated, this effect was most prominent at the larger flow rates but, even for the case with $R = 36.6$, did not appear to be a dominating factor. Thus, for example, in all experiments, the free surface in the central 40% of the channel was flat, in the cross-channel direction, to within 1% of the surface deflection at that location. Even for the flow at $R = 36.6$, where the most significant cross-channel variations were encountered, the non-uniformity amounted to no more than 10% of the surface displacement, with the maximum or minimum points for the cross-channel surface elevation being within a distance of 25 or 30% of the half-width of the channel from the side walls.

5. Concluding remarks

The comparisons described in this study were absolute ones, in the sense that there were no free parameters available with which to adjust the fit of the data. Therefore the close agreement, of the order of 2%, between the theoretical predictions and the experimental observations is as close as could reasonably be expected in view of the accuracies involved with the comparison. One aspect of the study of particular interest to us was the rather extensive range of applicability of the lubrication models. It seems clear from this study that such models have a valuable range of applicability, with the standard approximation providing a useful model for the observed flows up to Reynolds numbers of $O(1)$, and that, by making allowance for inertial effects, the range of applicability was expanded by nearly an order of magnitude in R.

Numerical solutions to the full problem were obtained only up to a Reynolds number of approximately 25. We are not sure why solutions beyond this Reynolds number were not obtainable, but it is possible that the difficulties are linked to a bifurcation near $R = 25$ to another steady flow, or to an unsteady motion. There is some experimental evidence that the flow was not completely steady in the cases with $R = 31.4$ and 36.6 near the place where the free surface reached its greatest slope.

The work of L.R.S. was supported in part by the National Science Foundation through award number DMS-8903548. The work of W.G.P. and S.J.T. was supported in part by the National Science Foundation through award number DMS-8805311-04 and DMS-9104518. We are indebted to Mr J. K. Bartington for constructing the experimental apparatus. We thank T. B. Benjamin for valuable suggestions and encouragement.

References

Abergel, F. & Bona, J. L. 1992 A mathematical theory for viscous free-surface flows over a perturbed plane. *Arch. ration. Mech. Analysis*. (In the press.)

Amick, C. J. 1977 Steady solutions of the Navier–Stokes equations in unbounded channels and pipes. *Ann. Scuola Norm. Sup. Pisa, IV* **4**, 473.

Amick, C. J. 1978 Properties of steady Navier–Stokes solutions for certain unbounded channels and pipes. *Nonlinear Analysis* **2**, 689.

Amick, C. J. & Fraenkel, L. E. 1980 Steady solutions of the Navier–Stokes equations representing plane flow in channels of various types. *Acta Mathematica* **144**, 83.

Ascher, U. M., Mattheij, R. M. M. & Russell, R. D. 1988 *Numerical solution of boundary value problems for ordinary differential equations*. Prentice Hall.

Bechtel, S. E., Forest, M. G., Holm, D. D. & Lin, K. J. 1988 One-dimensional closure models for three-dimensional incompressible viscoelastic free jets: von Kármán flow geometry and elliptical cross-section. *J. Fluid Mech.* **196**, 241.

Benjamin, T. B. 1957 Wave formation in laminar flow down an inclined plane. *J. Fluid Mech.* **2**, 554.

Bercovier, M. & Engelman, M. S. 1979 A finite element for incompressible fluid flows. *J. comp. Phys.* **30**, 181.

Brenner, S., Pritchard, W. G., Scott, L. R. & Tavener, S. J. 1992 The non-conforming Crouzeix Raviart element for computation of free-surface flows. (In preparation.)

Brezzi, F. & Falk, R. S. 1991 Stability of higher-order Hood–Taylor methods. *SIAM J. numer. Analysis* **28**, 581.

Ciarlet, P. G. 1978 *The finite element method for elliptic problems*. Amsterdam: North Holland.

Cliffe, A., Tavener, S. J. & Wheeler, A. 1992 An orthogonal mapping technique for the computation of a viscous free-surface flow. *Int. J. numer. Methods Fluids*. (In the press.)

Duran, R., Wang, J. & Nochetto, R. 1988 Sharp maximum norm error estimates for finite element approximations of the Stokes problem in 2-D. *Math. Comp.* **51**, 491.

Engelman, M. S. 1982 FIDAP – a fluid dynamics analysis package. *Adv. Engng Software* **4**, 163.

Girault, V. & Raviart, P.-A. 1986 *Finite element methods for Navier–Stokes equations*. Springer-Verlag.

Gunzburger, M. 1989 *Finite element methods for viscous incompressible flows*. Academic Press.

Hansen, E. B. 1986 Free surface Stokes flow over an obstacle. In *Boundary Elements VII Conference* (ed. M. Tanaka & C. A. Brebbia), p. 783. Springer-Verlag.

Hansen, E. B. 1987 Stokes flow down a wall into an infinite pool. *J. Fluid Mech.* **178**, 243.

Hasbani, I. & Engelman, M. S. 1979 Out of core solution of linear equations with non-symmetric coefficient matrix. *Comp. Fluids* **7**, 13.

Huppert, H. E. 1982*a* The propagation of two-dimensional and axisymmetric viscous gravity currents over a rigid horizontal surface. *J. Fluid Mech.* **121**, 43.

Huppert, H. E. 1982*b* Flow and instability of a viscous current down a slope. *Nature, Lond.* **300**, 427.

Jean, M. 1980 Free surface of the steady flow of a Newtonian fluid in a finite channel. *Arch. ration. Mech. Analysis* **74**, 197.

Johnson, R. E. 1988 Steady-state coating flows inside a rotating horizontal cylinder. *J. Fluid Mech.* **190**, 321.

Kopal, Z. 1955 *Numerical analysis*. New York: Wiley.

Landau, L. D. & Lifschitz, E. M. 1959 *Fluid dynamics*. Oxford: Pergammon.

Manton, M. J. 1971 Low Reynolds number flow in slowly varying axisymmetric tubes. *J. Fluid Mech.* **49**, 451.

Moffatt, H. K. 1977 Behaviour of a viscous film on the outer surface of a rotating cylinder. *J. Méc.* **16**, 651.

Pozrikidis, C. 1988 The flow of a liquid film along a periodic wall. *J. Fluid Mech.* **188**, 275.

Preziosi, L. & Joseph, D. D. 1987 Stability of rigid motions and coating films in bicomponent flows of immiscible liquids. *J. Fluid Mech.* **185**, 323.

Preziosi, L. & Joseph, D. D. 1988 The run-off condition for coating and rimming flows. *J. Fluid Mech.* **187**, 99.

Pritchard, W. G. 1986 Instability and chaotic behaviour in a free-surface flow. *J. Fluid Mech.* **165**, 1.

Pritchard, W. G., Saavedra, P., Scott, L. R. & Tavener, S. J. 1992 Theoretical issues arising in the modeling of viscous free-surface flows. *Free boundaries in viscous flows* (ed. R. Brown, S. Davis & S. Kistler). Springer-Verlag.

Saavedra, P. & Scott, L. R. 1991 Variational formulation of a model free-boundary problem. *Math. Comp.* **57**, 451.

Saito, H. & Scriven, L. E. 1981 Study of coating flow by the finite element method. *J. comp. Phys.* **42**, 53.

Shih, S. M. & Shen, M. C. 1975 Uniform asymptotic approximation for viscous fluid flow down an inclined plane. *SIAM J. math. Analysis* **6**, 560.

Solonnikov, V. A. 1980 Solvability of a problem in the plane motion of a heavy viscous incompressible capillary liquid partially filling a container. *Math. USSR Izvestia* **14**, 193.

Solonnikov, V. A. & Shchadilov, V. E. 1973 On a boundary value problem for a stationary system of Navier–Stokes equations. *Proc. Steklov Inst. Math.* **125**, 186.

Taylor, C. & Hood, P. 1973 A numerical solution of the Navier–Stokes equations using the finite element technique. *Computers Fluids* **1**, 73.

Whittaker, E. T. & Robinson, G. 1944 *Calculus of observations*, 4th edn. London: Blackie & Son.

Yih, C.-S. 1963 Stability of liquid flow down an inclined plane. *Phys. Fluids* **6**, 321.

Yih, C.-S. 1969 *Fluid mechanics*. Ann Arbor: West River Press.

Received 10 July 1991; revised 23 October 1991; accepted 18 February 1992

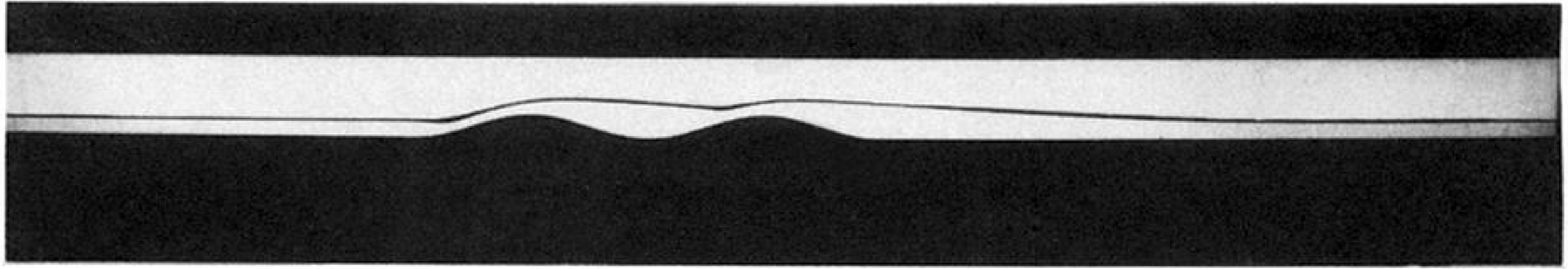

igure 1. A photograph indicating the free-surface profile for flow at a Reynolds number of pproximately 12. The flow is from right to left. The free surface of the liquid in the central portion f the channel is indicated by the lower edge of the thin line which derives from the meniscus on e side wall of the channel; the slight thickening of this line on the leeward side of the humps dicates the presence of some local structure near the side walls of the channel. The distance etween the crests of the two humps in the channel bed is 100 mm.